

**Elucidating the Mechanistic Origin of a Spin-State
Dependent Fe_{Nx}-C Catalyst toward Organic Contaminant
Oxidation via Peroxymonosulfate Activation**

ZHANG, Bofan, LI, Xianquang, AKIYAMA, Kazuhiko, BINGHAM, Paul
<<http://orcid.org/0000-0001-6017-0798>> and KUBUKI, Shiro

Available from Sheffield Hallam University Research Archive (SHURA) at:

<https://shura.shu.ac.uk/29459/>

This document is the Accepted Version [AM]

Citation:

ZHANG, Bofan, LI, Xianquang, AKIYAMA, Kazuhiko, BINGHAM, Paul and KUBUKI, Shiro (2021). Elucidating the Mechanistic Origin of a Spin-State Dependent Fe_{Nx}-C Catalyst toward Organic Contaminant Oxidation via Peroxymonosulfate Activation. Environmental Science and Technology. [Article]

Copyright and re-use policy

See <http://shura.shu.ac.uk/information.html>

Elucidating Mechanistic Origin of Spin-States Dependent FeN_x-C Catalyst towards Organic Contaminants Oxidation via Peroxymonosulfate Activation

Bofan Zhang^{1,†,*}, Xianquan Li^{2,†}, Kazuhiko Akiyama¹, Paul A. Bingham³, Shiro Kubuki¹

¹Department of Chemistry, Tokyo Metropolitan University, Tokyo 192-0397, Japan

²Dalian Institute of Chemical Physics, Chinese Academy of Sciences, Dalian 116023, China

³College of Business, Technology and Engineering, Sheffield Hallam University, Howard Street,
Sheffield S1 1WB, UK

*Corresponding authors: Bofan Zhang;

E-mail: 15054218031@163.com (B.F. Zhang)

† These authors contributed equally

This supplementary material includes 48 pages (including this page), 5 Texts, 7 Tables, and 26 Figures.

List of Supporting Information

Text S1. Chemicals

Text S2. Synthesis of FeN_x-C Catalysts

Text S3. Characterization

Text S4. Evaluation of Catalytic activity

Text S5. Computational Details

Figure S1. XRD patterns of the as-prepared FeN_x-C-5-500, FeN_x-C-5-600 and FeN_x-C-5-700 catalysts

Figure S2. XRD patterns of the as-prepared FeN_x-C-3-600 and FeN_x-C-7-600 catalysts

Figure S3. TG curves of Fe-MOF/melamine precursor in N₂ atmosphere

Figure S4. SEM images of as-synthesized catalysts

Figure S5. TEM images and EDS mapping of FeN_x-C-700 catalyst

Figure S6. Raman spectra of as-synthesized catalysts

Figure S7. N₂ adsorption-desorption isotherm and pore size distribution of as-synthesized catalysts

Figure S8. Fe 2p XPS spectra of FeN_x-C-500, FeN_x-C-600 and FeN_x-C-700 catalysts

Figure S9. N 1s XPS spectra of FeN_x-C catalysts and the relative ratio of different N species

Figure S10. (a) Fe K-edge XANES spectra (b) Relation between the Fe K-edge absorption energy and valence states for FeN_x-C and reference mater; (c) Wavelet transform plots of FeN_x-C-600, Fe₂O₃, Fe foil and FePc samples

Figure S11. Atomic structure and calculated formation energy of (a) Fe-pyridinic N₄; (b) Fe-pyrrolic N₄ and (c) Fe-graphitic N₄

Figure S12. Low temperature ⁵⁷Fe Mössbauer spectra (77K) of sample FeN_x-C-600

Figure S13. (a) Adsorption ability of FeN_x-C-500/600/700 catalysts; (b) Degradation efficiency; (c-d) Degradation rate and TOC removal rate of various organic pollutants via FeN_x-C-600 catalyst

Figure S14. Influence of (a) pH, (b) TOC removal rate under different pH conditions, (c) Influence of the Fe-MOF/melamine ratio in precursors, (d) PMS dosage and (e) FeN_x-C-600 catalyst dosage on BPA degradation in the FeN_x-C-600/PMS system

Figure S15. Pseudo-first-order kinetics of degradation of MB in different influencing factors of the FeN_x-C-600 catalyst

Figure S16. MS spectra of BPA decomposition in FeN_x-C-600/PMS system at different times

Figure S17. Proposed degradation pathways of BPA in the FeN_x-C-600/PMS system

Figure S18. (a-b) Influence of various scavenging agents on BPA degradation; (c) DMPO-trapped EPR spectra of O₂^{•-} radicals in the FeN_x-C-600/PMS system

Figure S19. Influence of Oxalate, FeCl₂ and Fe(NO₃)₃ on BPA degradation

Figure S20. Catalytic activity, XRD pattern and TEM image of FeN_x-C-600 after HCl poisoned

Figure S21. (a-d) PMSO consumption and PMSO₂ generation in the FeN_x-C-600/PMS/BPA system, (e-f) MS/MS spectra of PMSO and PMSO₂, (g-h) MS spectra of PMS¹⁶O¹⁶O/ PMS¹⁶O¹⁸O in FeN_x-C/PMS system and (i-j) MS spectra of PMS¹⁶O¹⁶O in PMS alone system

Figure S22. Fitted ⁵⁷Fe Mössbauer spectra of as-synthesized catalysts and the correlation between high spin ferric iron sites and catalytic activity

Figure S23. (a) EPR spectra of sample FeN_x-C-600 in distilled water and PMS solution under 77K; (b) EIS Nyquist plots of FeN_x-C-500, 600 and 700 catalysts

Figure S24. (a) Fitted ⁵⁷Fe Mössbauer spectra of MIL-101(Fe) precursor; (b) XRD pattern of 101FeN_x-C-600 catalyst; (c) TEM images and EDS mapping of 101FeN_x-C-600 catalyst; (d) Catalytic performance for BPA degradation; (e) Stability of 101FeN_x-C-600 for BPA removal

Figure S25. (a) Fe 2p and (b) N 1s XPS spectra of used FeN_x-C-600 catalyst; (c-d) *HSO₅ in different reaction process: (c) in Figure 5(c) *HSO₅-1; (b) in Figure 5(d) *HSO₅-2

Figure S26. (a) Cycling experiment for BPA degradation; (b) XRD pattern; (c) FTIR spectra of FeN_x-C-600 catalyst; (d) Catalytic performance of leached iron towards BPA degradation; (e) BPA removal rate in tap water; (f) BPA removal rate in actual wastewater; (g) TOC removal rate in actual wastewater by FeN_x-C-600 catalyst over five cycles

Table S1. Structures and measurement parameters of various organic pollutants

Table S2. Iron content measured by ICP-OES and structural parameters of BET surface area, pore volume and pore size

Table S3. Structural parameters of the FeN_x-C-600 catalysts obtained from EXAFS fitting

Table S4. MS analysis of reaction intermediates during the degradation of BPA

Table S5. Comparison of catalytic reactivity of FeN_x-C-600 catalyst with previous reported catalysts during PMS activation

Table S6. Parameters of industrial wastewater sample

Table S7. Summary of the fitted ⁵⁷Fe Mössbauer parameters and assignments to different Fe species

S1. Chemicals

$\text{FeCl}_3 \cdot 6\text{H}_2\text{O}$, $\text{Bi}(\text{NO}_3)_3 \cdot 5\text{H}_2\text{O}$, 1,4-benzenedicarboxylic acid (1,4-BDC), potassium iodide, N,N-dimethylformamide (DMF), melamine, methanol (MeOH), sodium azide (NaN_3), tert-Butyl Alcohol (TBA), absolute ethanol, p-benzoquinone, triethanolamine, and isopropyl alcohol were purchased from Siyaku Chemical Reagent Co., Ltd., Japan. All reagents used were analytical grade reagents.

S2. Synthesis of $\text{FeN}_x\text{-C}$ Catalysts

In a typical synthesis, the Fe-MOF was mixed with melamine at a mass ratio of 1:3, 1:5 and 1:7, and then fully ground in an agate mortar. After that, the mixture was transformed into a quartz boat and then placed in a tube furnace. Before calcination, the tube furnace was purged with nitrogen (N_2) for 30 min and then the mixture was calcined for 3 hours at 500, 600 and 700 °C under N_2 flow. After cooling naturally to room temperature, the final iron-based catalysts (marked as $\text{FeN}_x\text{-C-X-T}$, $X=3, 5, 7$; $T=500, 600, 700$) were obtained. Additionally, the metal-free N-C catalyst (NC) was also prepared with the similar process without addition of iron source.

S3. Characterization

X-ray diffraction (XRD) patterns were obtained from an X-ray diffractometer with $\text{Cu K}\alpha$ radiation, then were applied to evaluate the crystal structure of the samples. The Fourier transform-infrared (FT-IR) spectra were obtained using an FT-IR optical spectrometer (Nexus 670) in the range $500\text{-}3500\text{ cm}^{-1}$. The morphology and composition of catalysts were analyzed by transmission electron microscopy (TEM, JEM-3200FS) and energy-dispersive X-ray spectroscopy (EDX). Atomic-resolution high-angle annular dark-field scanning TEM (HAADF-STEM) images were recorded by FEI Theims Z measurement. The X-ray absorption fine structure spectra (Fe-K edge) were measured on the 1W1B station in Beijing Synchrotron Radiation Facility (BSRF). Data were

collected through a fixed-exit double-crystal Si (111) monochromator. The obtained data were analyzed by Athena and Artemis. Surface electronic states were recorded by X-ray photoelectron spectroscopy (XPS, VG MultiLab 2000). The N₂ adsorption-desorption measurements were analyzed by the nitrogen adsorption apparatus (ASAP 2020, USA). Electrochemical impedance spectroscopy (EIS) and current-voltage curve (CV) were analyzed in a three-electrode system of the CHI-600E electrochemical workstation (Shanghai Chenhua, China). The total organic carbon (TOC) was analyzed using a multi N/C 3100 analyzer. ⁵⁷Fe Mössbauer spectra of Fe-MOF and FeN_x-C catalysts were obtained using ⁵⁷Co (Rh) γ -ray radioactive source maintained at room temperature (298 K) and low temperature (77 K). EPR spectra were recorded using a Bruker ESR A300-10/12 spectrometer at room temperature and low temperature (77 K).

For the detection of PMSO and PMSO₂ molecules, Liquid chromatography was performed using an ACQUITY UPLC System (Waters Corp., Milford, USA). The analytical column used were HSS-3 column (2.1×100 mm, 5 μ m particle diameter) maintained at 30 °C. Mobile phase A and B are water and acetonitrile containing 0.1% formic acid, respectively. Samples (1 μ L) were injected and analyzed under isocratic condition consisting different concentration of mobile phase B at a flow rate of 0.5 mL/min. LC-MS/MS analysis was performed on AB Sciex Qtrap® 5500 instrument (AB Sciex Pte. Ltd, Foster City, CA) with an ESI Turbo V ion spray source operating in positive mode and detected by multiple reaction monitoring (MRM). Nitrogen was the only gas used. The ion spray voltage was set at 5500 V, source temperature at 550 °C, curtain gas (CUR) at 25 psi, nebulizer gas (GS1) at 60 psi, and de-solvation gas (GS2) at 70 psi. Collision gas (CAD) was set at Medium. Compound related MS parameters were set as follows: ion pair 141.1/123.9 was detected for PMSO, while 156.8/79.0 was monitored for PMSO₂. Dwell time was set at 50 ms for all ion pairs. The de-clustering potential (DP) was set at 60 V for PMSO and 40 V for PMSO₂,

collision energy (CE) at 25 V for PMSO and 15 V for PMSO₂, entrance potential (EP) at 10 V and collision exit potential (CXP) at 13 V. Signal acquisition and peak integration were performed via Analyst® 1.6 software.

S4. Evaluation of Catalytic activity

The catalytic activity of as-synthesized catalysts was measured via decomposition of bisphenol A (BPA), phenol, methylene blue (MB), Rhodamine B (RhB) and carbamazepine (CBZ). Specifically, 0.2 g/L catalyst was first added into 20 mg/L BPA solution and stirred for 60 min to establish absorption–desorption equilibrium. After that, the Fenton-like reaction was initiated by adding 0.5 mM PMS solution. As the reaction proceeded, 0.3 mL aliquots were withdrawn at certain time intervals and then measured by high-performance liquid chromatography (HPLC). The detailed detection methods for BPA, phenol, MB, RhB, CBZ are shown in Table S1.

S5. Computational Details

Density functional theory (DFT) calculations were performed to calculate the spin-polarization density using the Perdew-Burke-Ernzerhof (PBE) formulation¹⁸. The projected augmented wave (PAW) potentials¹⁹ and a plane wave basis with a kinetic energy cutoff of 450 eV were used to describe the ionic cores and valence electrons. The adsorption energies (E_{ads}) and free energy (ΔG) for reaction steps were also calculated.

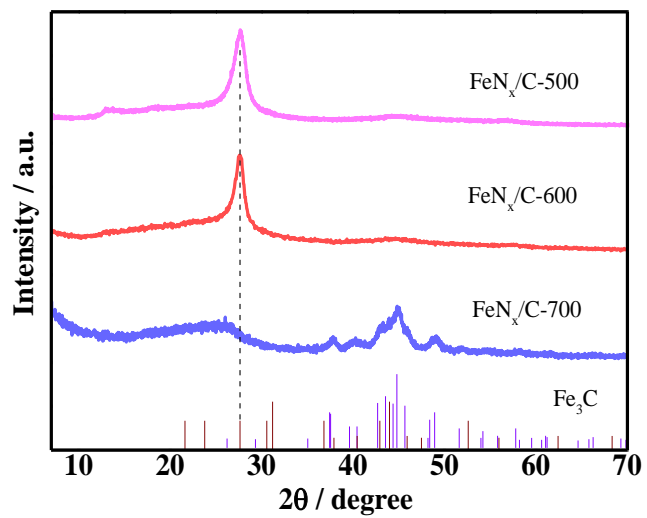


Figure S1. XRD patterns of the as-prepared FeN_x-C-5-500, FeN_x-C-5-600 and FeN_x-C-5-700 catalysts

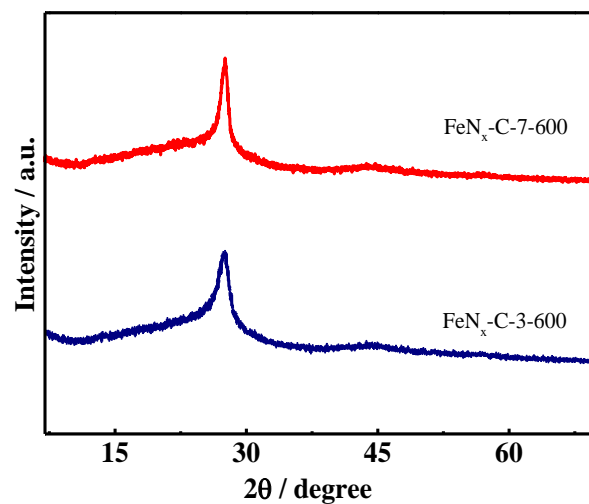


Figure S2. XRD patterns of the as-prepared FeN_x-C-3-600 and FeN_x-C-7-600 catalysts

The X-ray diffraction pattern (XRD) of the FeN_x-C-3-600 and FeN_x-C-7-600 samples also only exhibited two representative peaks located at 27.5 and 44.5°, which were assigned to the graphitic carbon (JCPDS No. 46-0945). These results are in accordance with the FeN_x-C-5-600 material, indicating similar structures in these three samples.

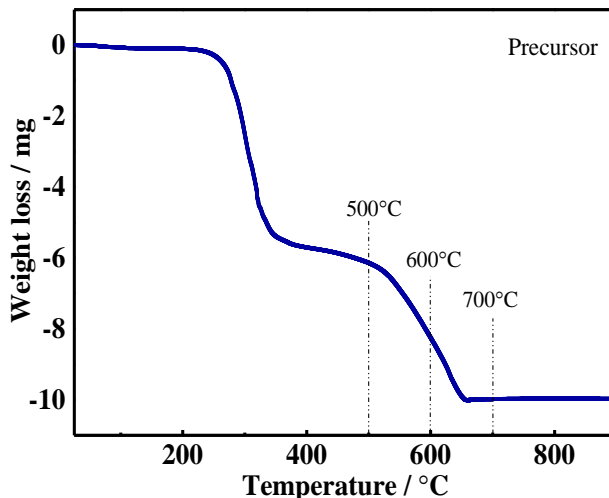


Figure S3. TG curves of Fe-MOF/melamine precursor in N₂ atmosphere

Thermogravimetric analysis (TGA) was performed to explore the pyrolysis process of FeN_xC-600 (Fe-MOF/melamine=1: 5). During pyrolysis, the slight mass loss at a temperature below 250 °C was due to the release of adsorbed water¹. Further increasing temperature led to catalyst decomposition, rapidly releasing iron species, and the final decomposition was completed at 665 °C. During this process, the structure of N-containing melamine could rearrange and generate the tri-*s*-triazine moiety, accompanied by the formation of reducing gas such as NH₃². Owing to the release of iron species in Fe-MOF and the strong coordination between N atoms and iron ions, the iron species can be efficiently captured by the melamine and tri-*s*-triazine molecules to generate active Fe-N_x species³. After the thermal calcination temperature (~665 °C), it was evidenced that the precursor converted into Fe₃C species verified by XRD analysis and ⁵⁷Fe Mössbauer spectra.

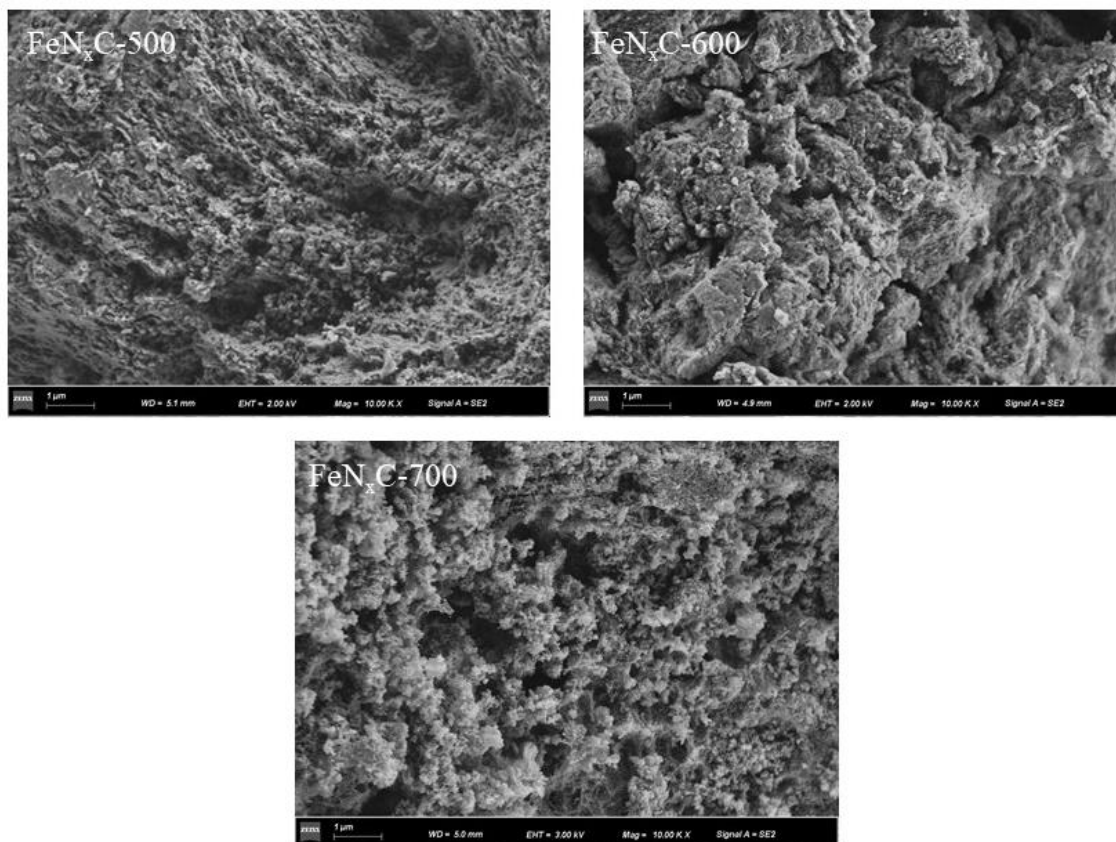


Figure S4. SEM images of as-synthesized catalysts

SEM images indicate similar sheet-like structural features with a large number of nanopores in the three catalysts. This porous structure is conducive to mass transport between catalyst and contaminant, thereby accelerating the kinetics of the Fenton-like reaction.

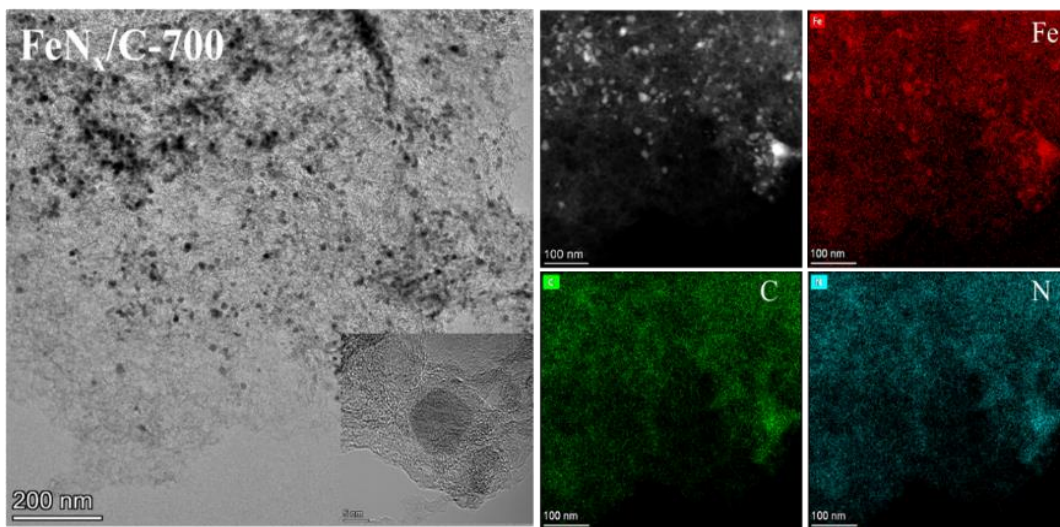


Figure S5. TEM images and EDS mapping of FeN_x-C-700 catalyst

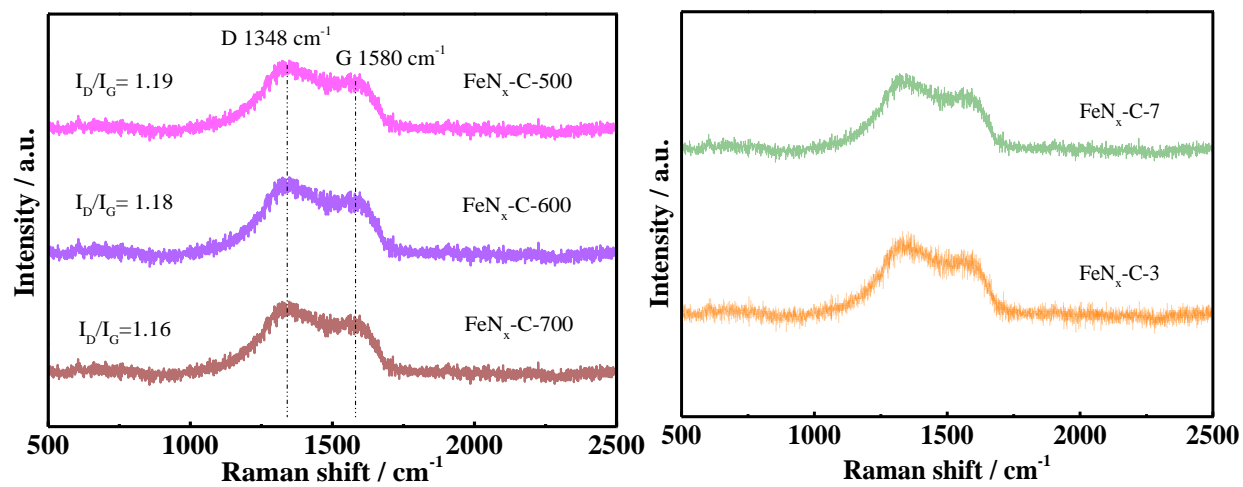


Figure S6. Raman spectra of as-synthesized catalysts

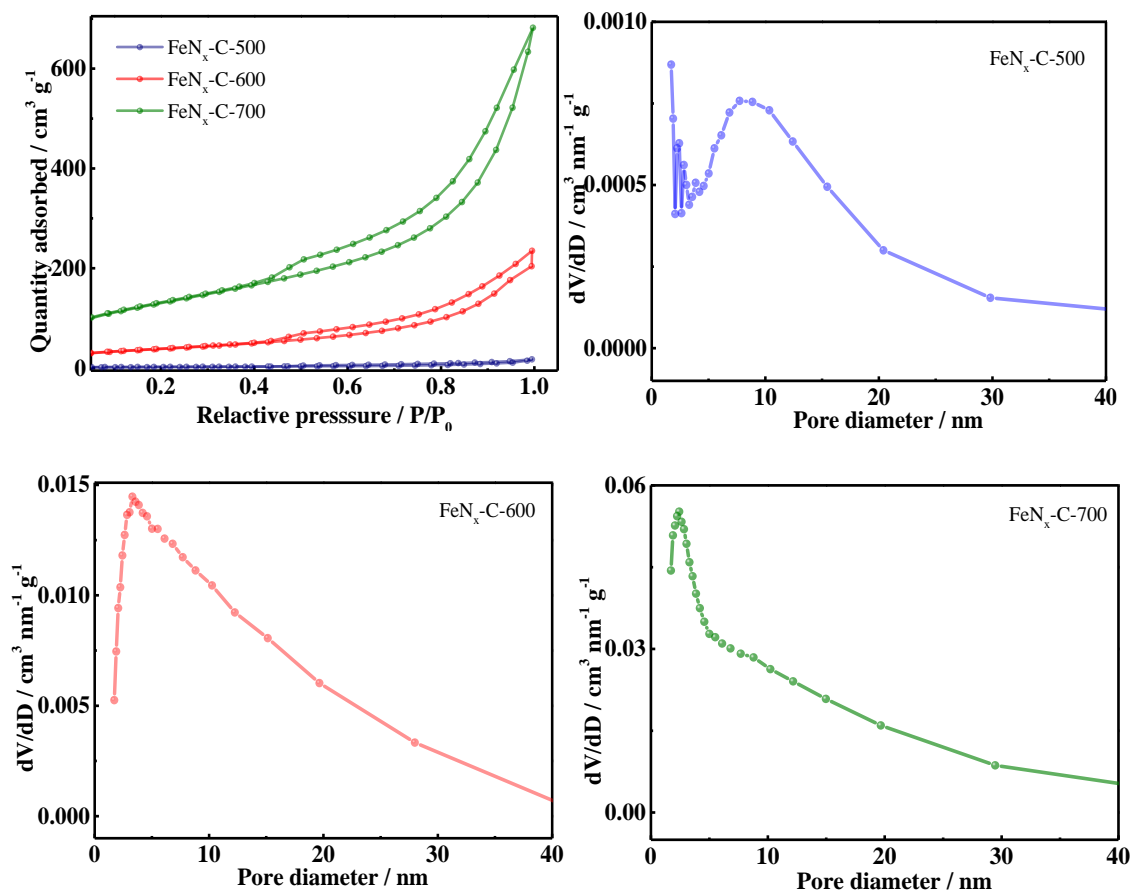


Figure S7. N₂ adsorption-desorption isotherm and pore size distribution of as-synthesized catalysts

The pore size distribution curves obtained from desorption branch by the Barrett-Joyner-Halenda model indicated that samples FeN_x-C-500/600/700 possessed uniform pore sizes of 8.23, 8.32 and 7.84 nm, respectively.

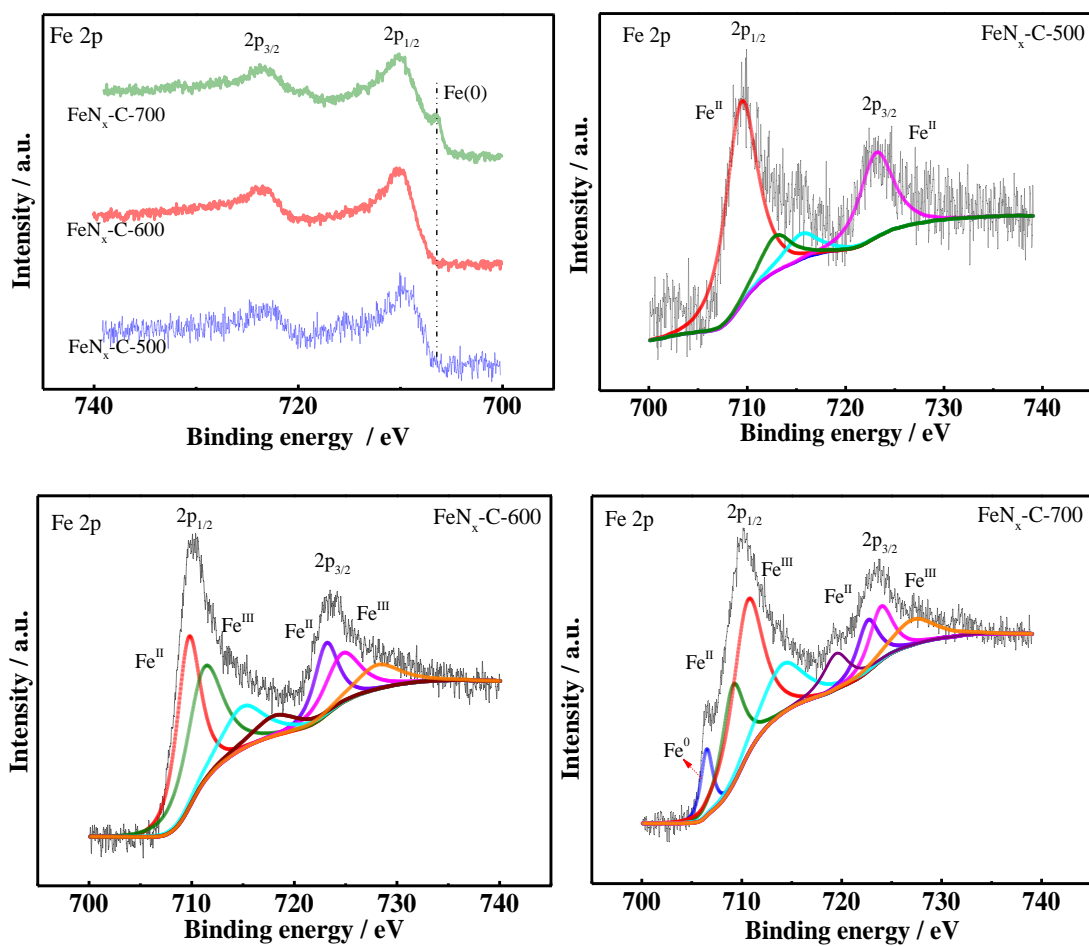


Figure S8. Fe 2p XPS spectra of FeN_x-C-500, FeN_x-C-600 and FeN_x-C-700 catalysts

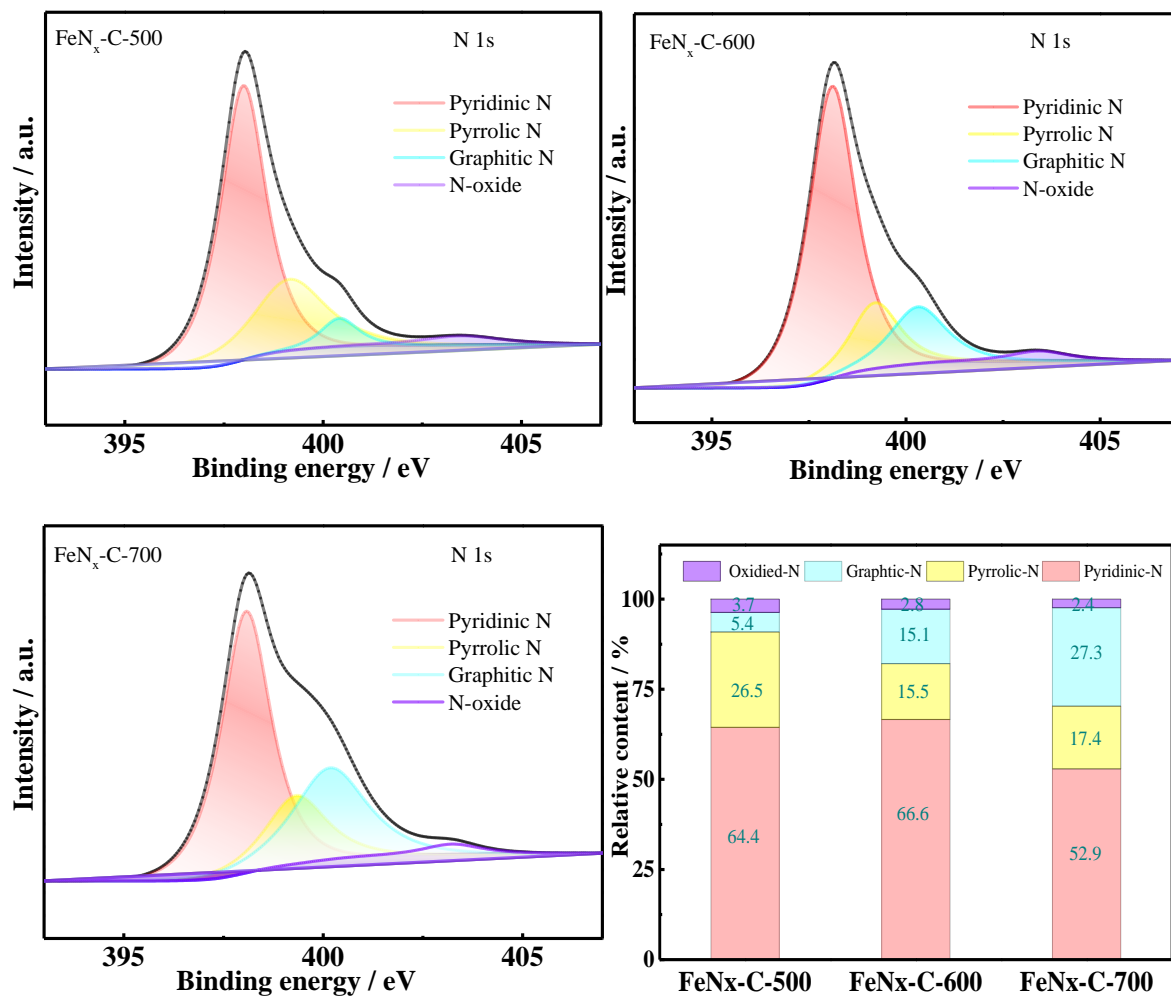


Figure S9. N 1s XPS spectra of FeN_x-C catalysts and the relative ratio of different N species

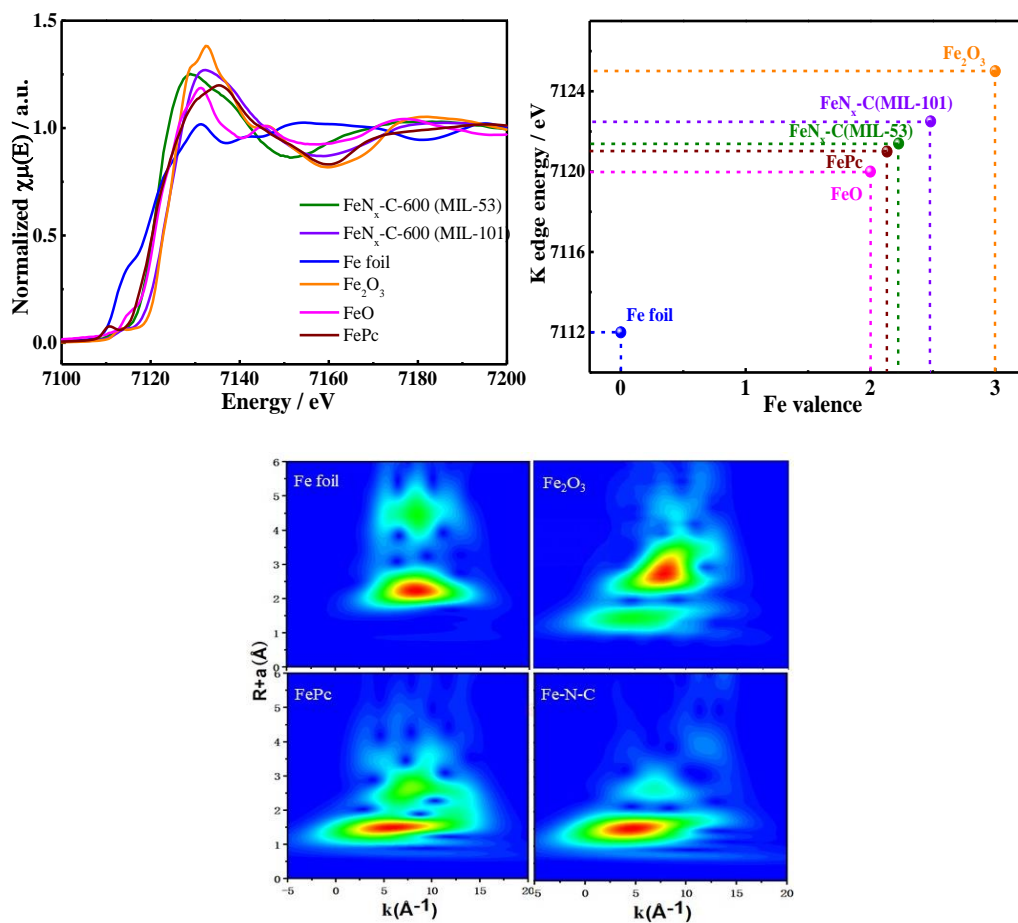


Figure S10. (a) Fe K-edge XANES spectra (b) Relation between the Fe K-edge absorption energy and valence states for FeN_x-C and reference mater; (c) Wavelet transform plots of FeN_x-C-600, Fe₂O₃, Fe foil and FePc samples

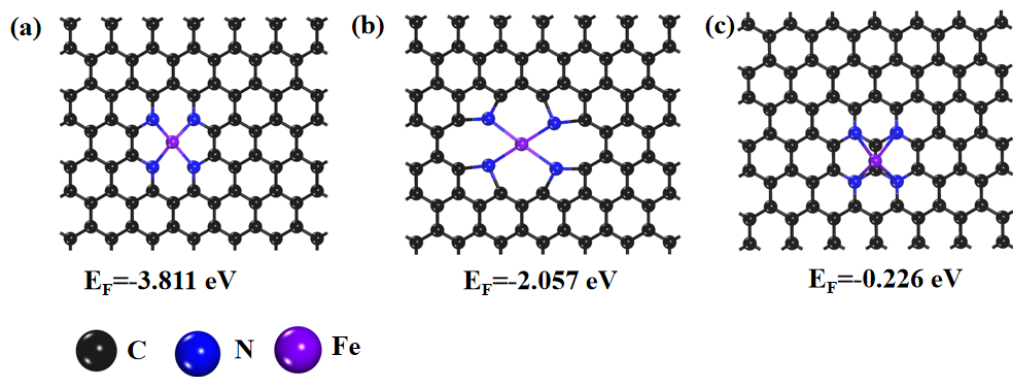


Figure S11. Atomic structure and calculated formation energy of (a) Fe-pyridinic N₄; (b) Fe-pyrrolic N₄ and (c) Fe-graphitic N₄

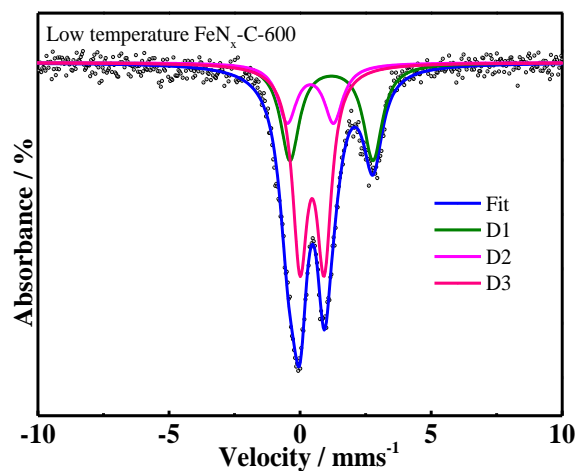


Figure S12. Low temperature ^{57}Fe Mössbauer spectra (77K) of sample $\text{FeN}_x\text{-C-600}$

The low temperature ^{57}Fe Mössbauer spectra can be also deconvoluted into three doublets. In comparison with ambient Mössbauer spectra, both isomer shift and quadrupole splitting values slightly increased owing to the deceleration in thermal motion upon cooling. These three doublets with similar parameters to those fitted to the ambient spectra can also be assigned to molecular FeN_4 -like sites with ferrous ions in high-spin (D1, $S=2$), ferric ions in high-spin (D2, $S=5/2$) and low-spin (D3, $S=1/2$) states, demonstrating the similar ambient space group symmetry and same local coordination environment of iron. Moreover, the low temperature ^{57}Fe Mössbauer spectra were devoid of any singlet or sextet assignable to nanometer-sized iron particles, ruling out the existence of measurable levels of iron oxides, iron carbide and zero-valent irons species in the $\text{FeN}_x\text{-C-600}$ catalyst.

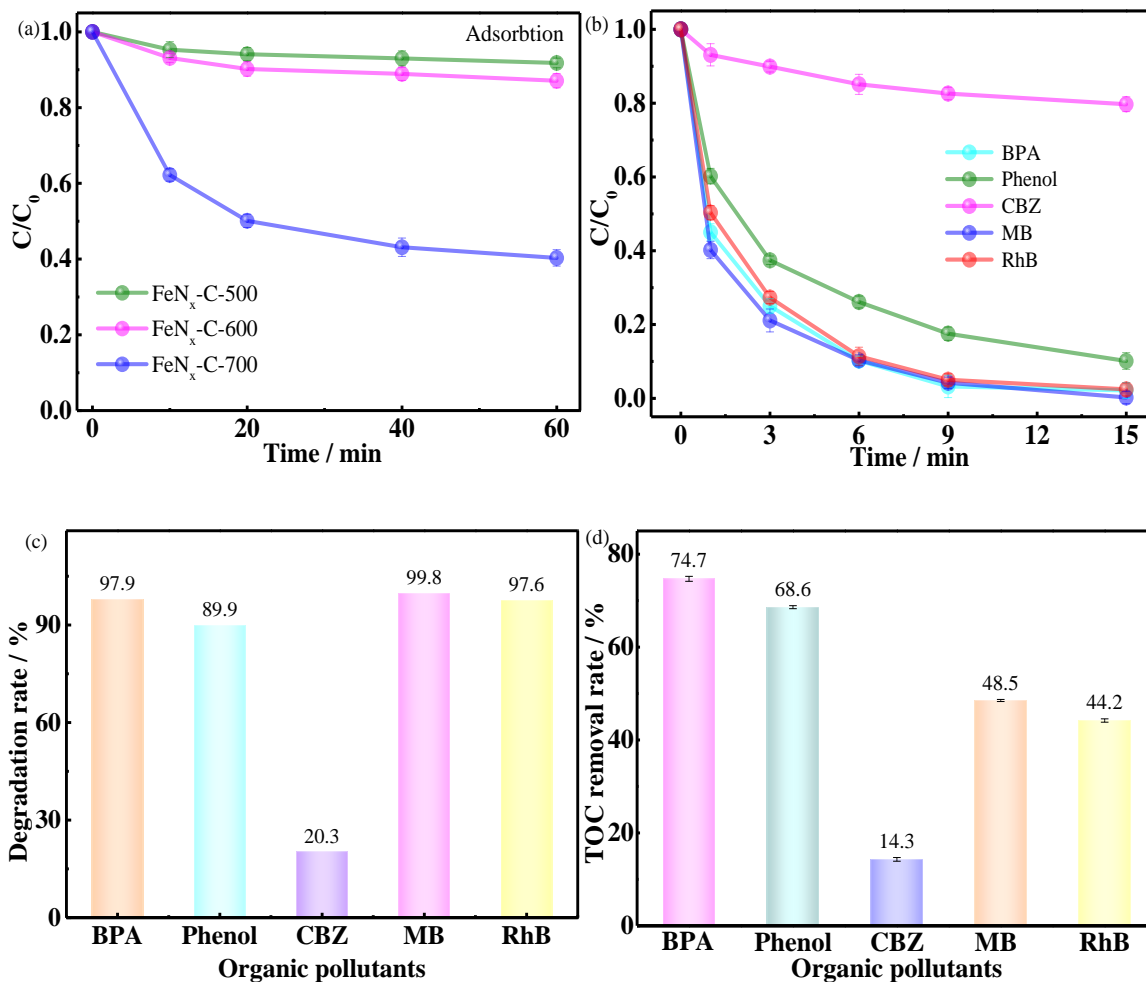


Figure S13. (a) Adsorption ability of Fe_{N_x}-C-500/600/700 catalysts; (b) Degradation efficiency; (c-d) Degradation rate and TOC removal rate of various organic pollutants via Fe_{N_x}-C-600 catalyst; Reaction conditions: catalyst dosage = 0.2 g/L, [PMS]₀ = 0.50 mM, [BPA]₀ = [phenol]₀ = [CBZ]₀ = [MB]₀ = [RhB]₀ = 20 mg/L, pH₀ = 6.5

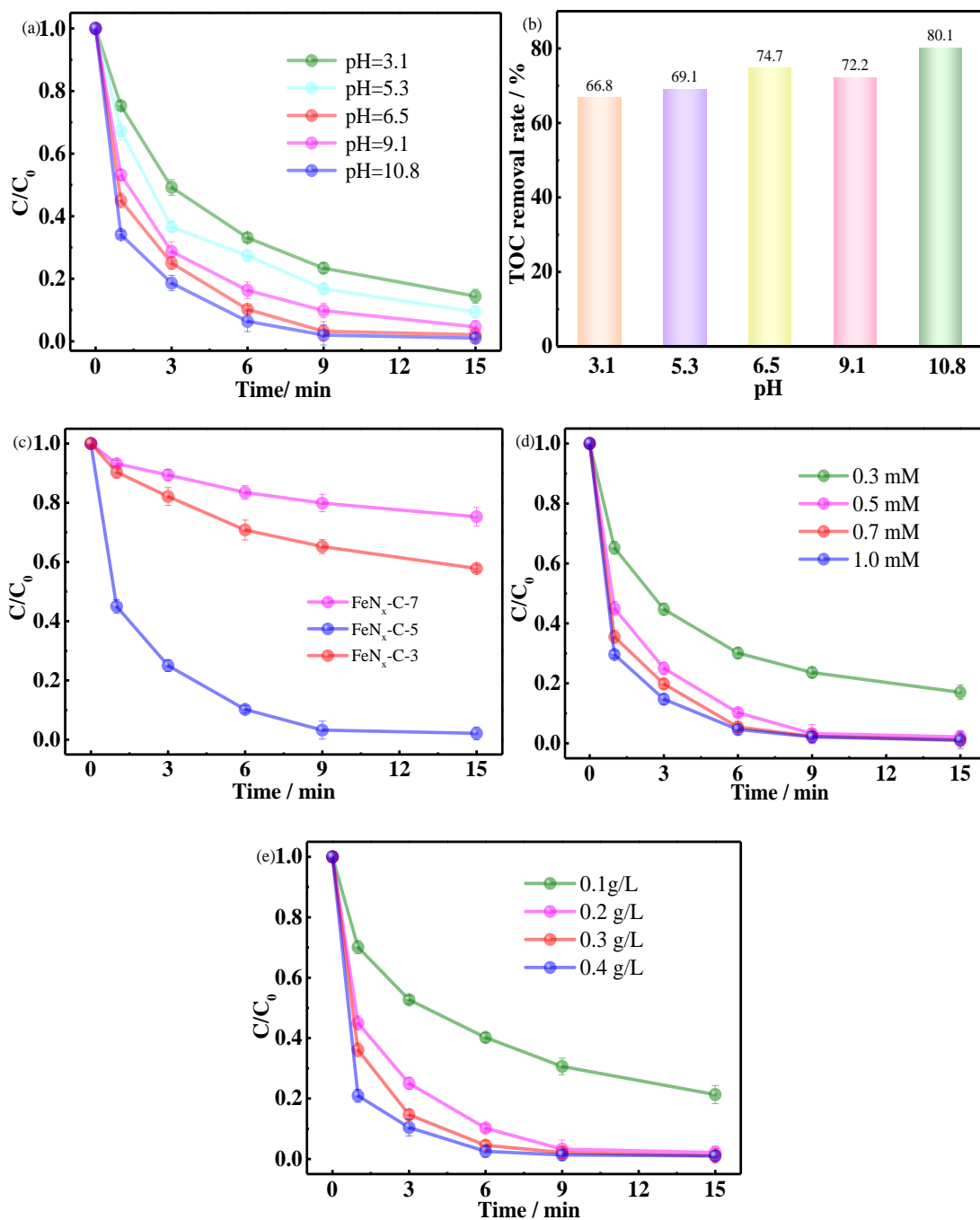


Figure S14. Influence of (a) pH, (b) TOC removal rate under different pH conditions, (c) Influence of the Fe-MOF/melamine ratio in precursors, (d) PMS dosage and (e) FeN_x-C-600 catalyst dosage on BPA degradation in the FeN_x-C-600/PMS system. Reaction conditions: catalyst dosage = 0.1-0.4 g/L, [PMS]₀ = 0.30-1.0 mM, [BPA]₀ = 20 mg/L, pH₀ = 3.1-10.8

To further achieve optimal reaction conditions and explore the most reactive catalyst, the influence of pH, PMS concentration, catalyst dosage and the initial ratio of Fe-MOF and melamine in the precursor were systematically explored. As shown in Figure S14a, in all conditions, degradation can be achieved more than 80% in only 15 min, illustrating a wide working pH range of FeN_x-C-600 catalyst. The highest efficiency was obtained in range of pH=6.5~10.8. In relatively acidic conditions, the presence of high proton concentrations inhibited the reaction of sulfate and hydroxyl radical with BPA pollutant since hydrogen ions could scavenge sulfate and hydroxyl radicals⁴. On the other hand, alkaline condition may give rise to the reaction proceed in the positive direction, which is conducive to the production of reactive species and improving catalytic ability. The total organic carbon (TOC) removal rates were also measured under different pH value, further illustrating the admirable catalytic reactivity of sample FeN_x-C-600 for BPA degradation. In comparison with FeN_x-C-3 and FeN_x-C-7 samples, FeN_x-C-5 catalyst showed the highest degradation rate toward BPA (Figure S11c). It indicated that appropriate amount of melamine could provide an optimal coordination environment between iron and nitrogen atoms, which played a significant role in PMS activation and organic pollutant decomposition. The catalytic efficiency can achieve 97.9% within 15 min under a PMS concentration of 0.5 mM (Fig. S11d), which only exhibited a slight decrease compared with 0.7 and 1.0 mM. Moreover, with the increase of catalyst dosage, more active sites can participate in the Fenton-like reaction and accelerate the oxidation of pollutants⁵. Nevertheless, it can be noticed that no significant improvement appeared between 0.2 g/L and 0.4 g/L. Considering the balance between catalytic performance and cost, a solution with an initial pH value of 6.5 containing 20 mg/L BPA, 0.5 mM PMS and a moderate catalyst dosage of 0.2 g/L was applied in the following experiments.

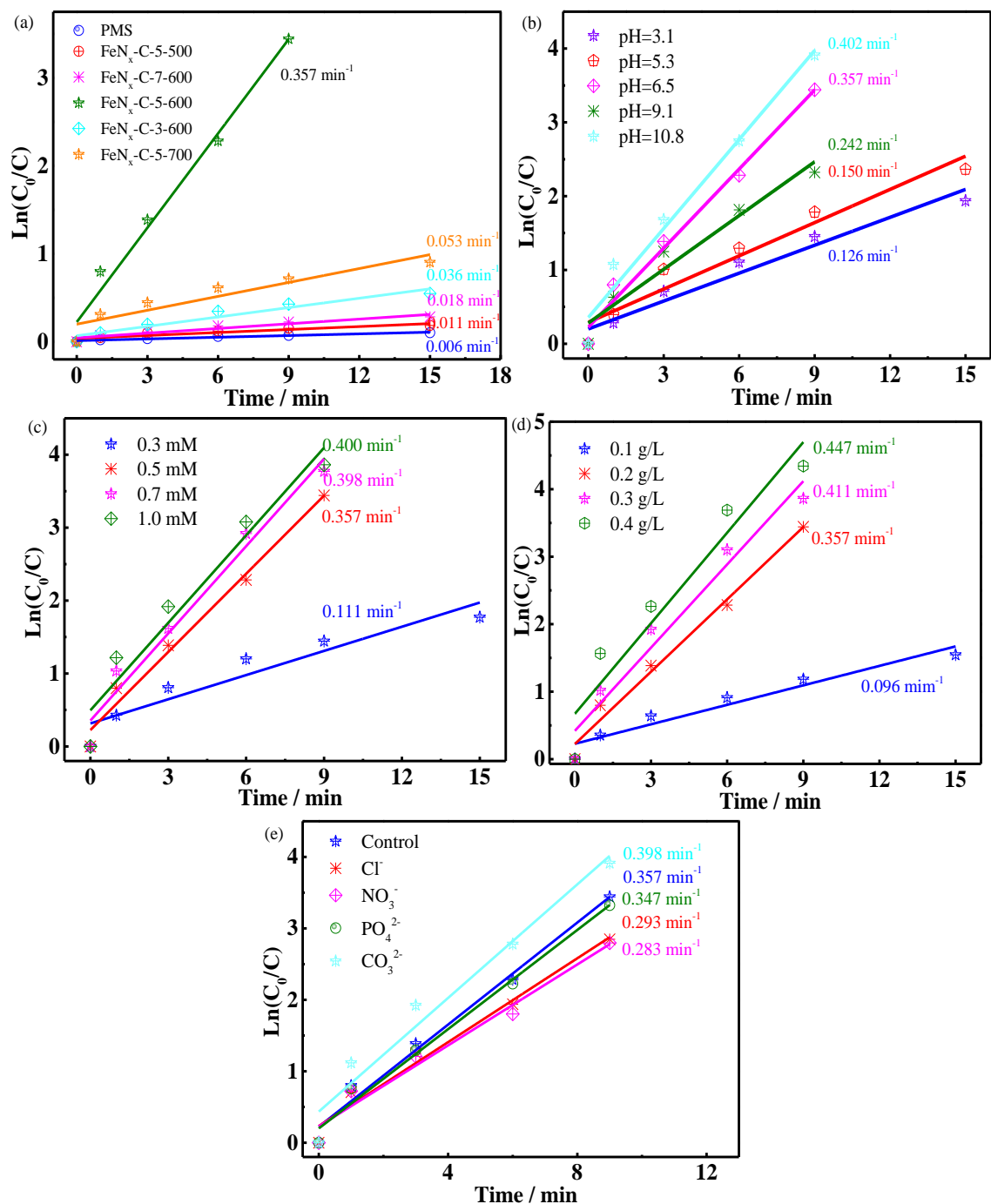


Figure S15. Pseudo-first-order kinetics of degradation of MB in different influencing factors of the Fe_xN_x-C-600 catalyst; Reaction conditions: catalyst dosage = 0.2 g/L, [PMS]₀ = 0.50 mM, [BPA]₀ = 20 mg/L, pH₀ = 6.5, [Cl⁻]₀ = [NO₃⁻]₀ = [PO₄²⁻]₀ = [CO₃²⁻]₀ = 10.0 mM

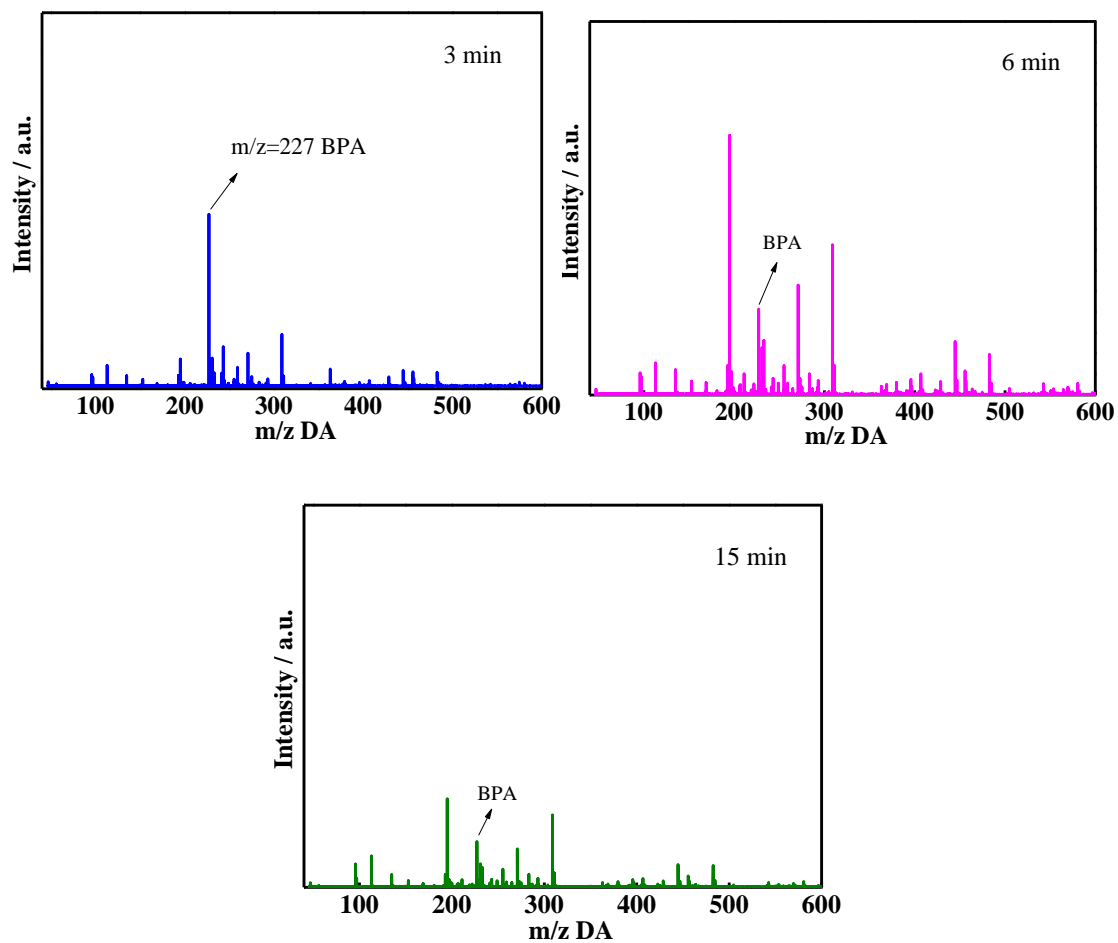


Figure S16. MS spectra of BPA decomposition in FeN_x-C-600/PMS system at different times

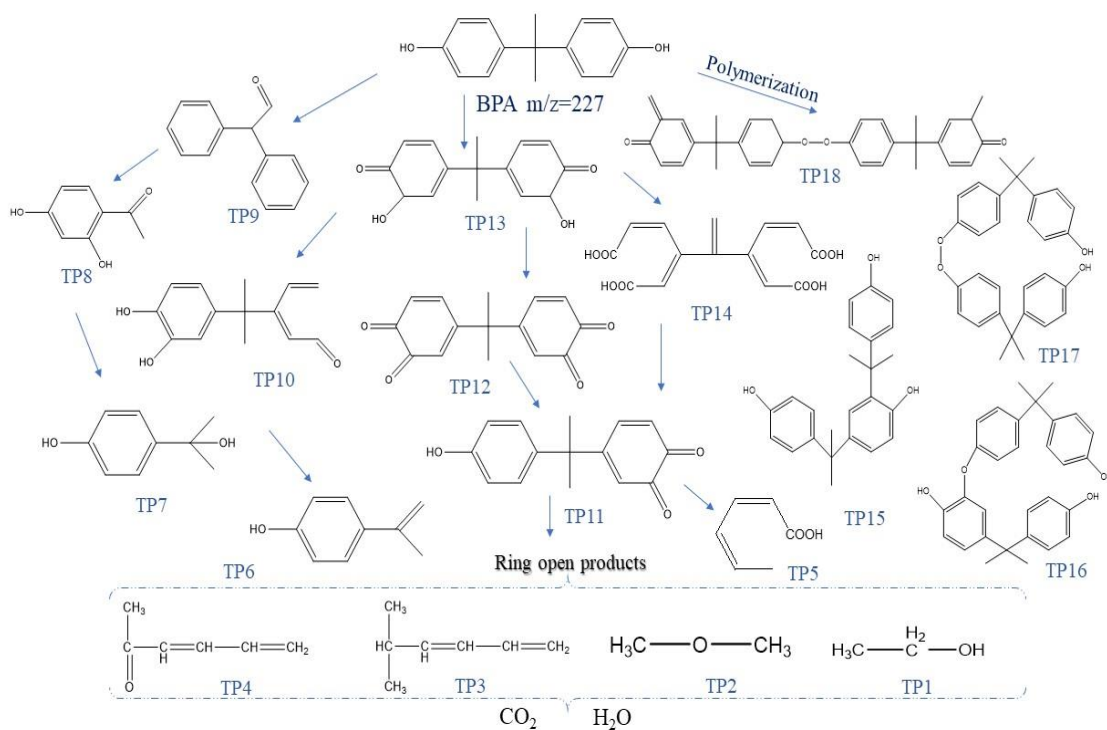


Figure S17. Proposed degradation pathways of BPA in the FeN_x-C-600/PMS system

As shown in Figure 3d, S16-17 and Table S1, the product with m/z of 227 is assigned to BPA substrate. As the degradation time increased, various ring-opening and polymerization intermediates were detected. Specifically, BPA can be first attacked by the formed reactive species to generate small molecules such as 2,2-diphenylethanone, 4-isopropylencatechol and 3,5-bis(1,1-dimethyl (ethyl)). Meanwhile, owing to the effect of dehydration and rearrangement of oxidative skeletal, various intermediates including TP11-14 were formed during the catalytic reaction. Moreover, larger molecular compounds such as TP16-18 were observed due to the polymerization of generated intermediates and could be also oxidized into small molecules over the next oxidation process. This is followed by further deep attack via ring-open and cleavage reaction, several micro-molecules such as TP1-4 were produced and then expected to be finally mineralized into CO₂ and H₂O.

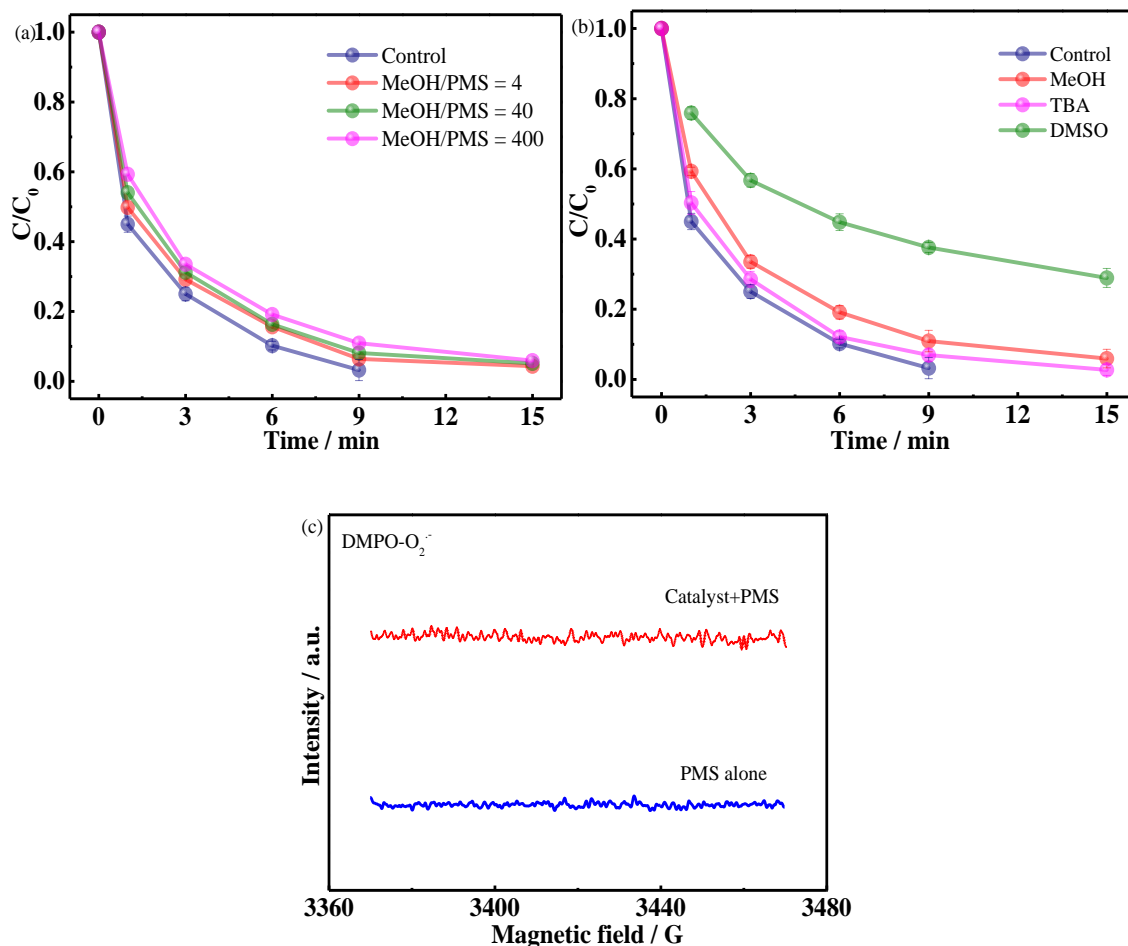


Figure S18. (a-b) Influence of various scavenging agents on BPA degradation; (c) DMPO-trapped EPR spectra of $O_2^{\bullet-}$ radicals in the FeN_x -C-600/PMS system; Reaction conditions: catalyst dosage = 0.2 g/L, $[PMS]_0 = 0.50$ mM, $[BPA]_0 = 20$ mg/L, $pH_0 = 6.5$, $[TBA] = 100$ mM, $[DMSO] = 1.0$ mM

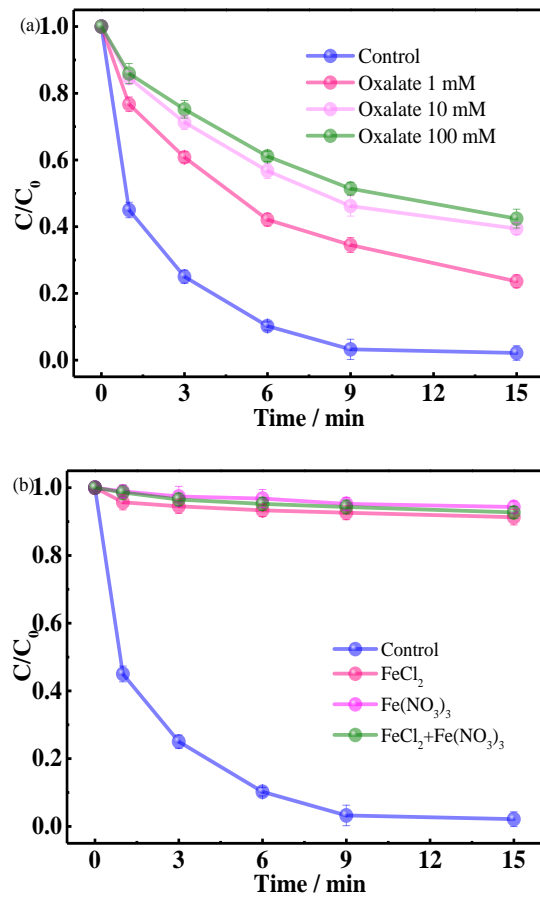


Figure S19. Influence of Oxalate, FeCl₂ and Fe(NO₃)₃ on BPA degradation, Reaction conditions: catalyst

dosage = 0.2 g/L, [PMS]₀ = 0.50 mM, [BPA]₀ = 20 mg/L, pH₀ = 6.5, oxalate = 1-100 mM

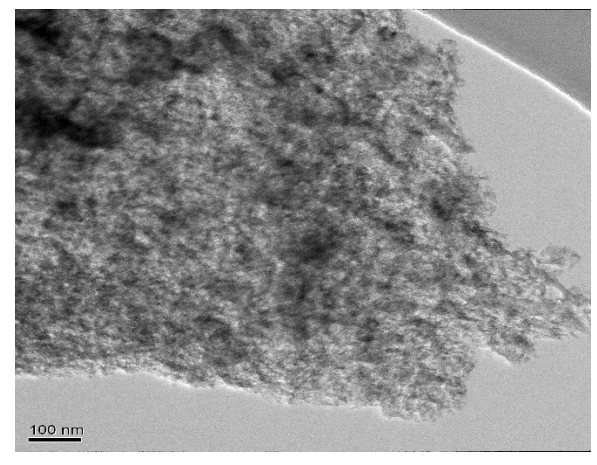
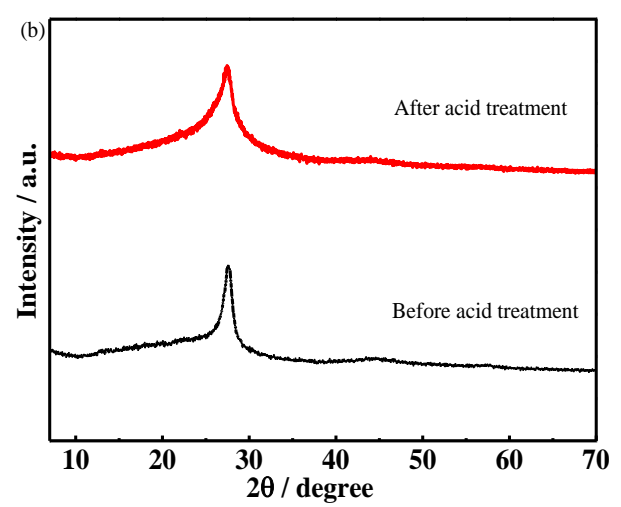
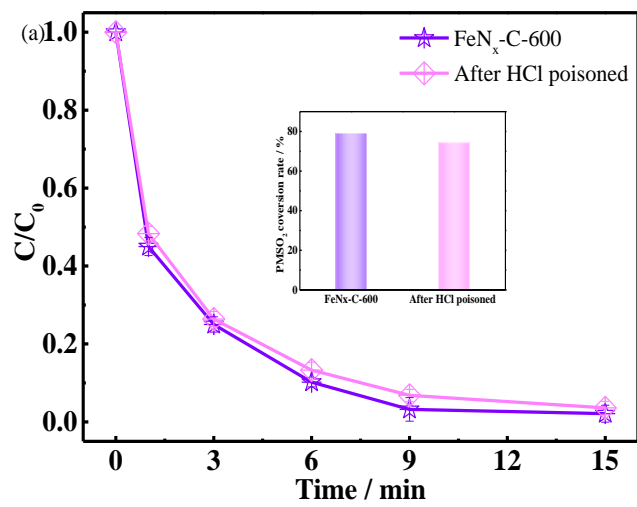
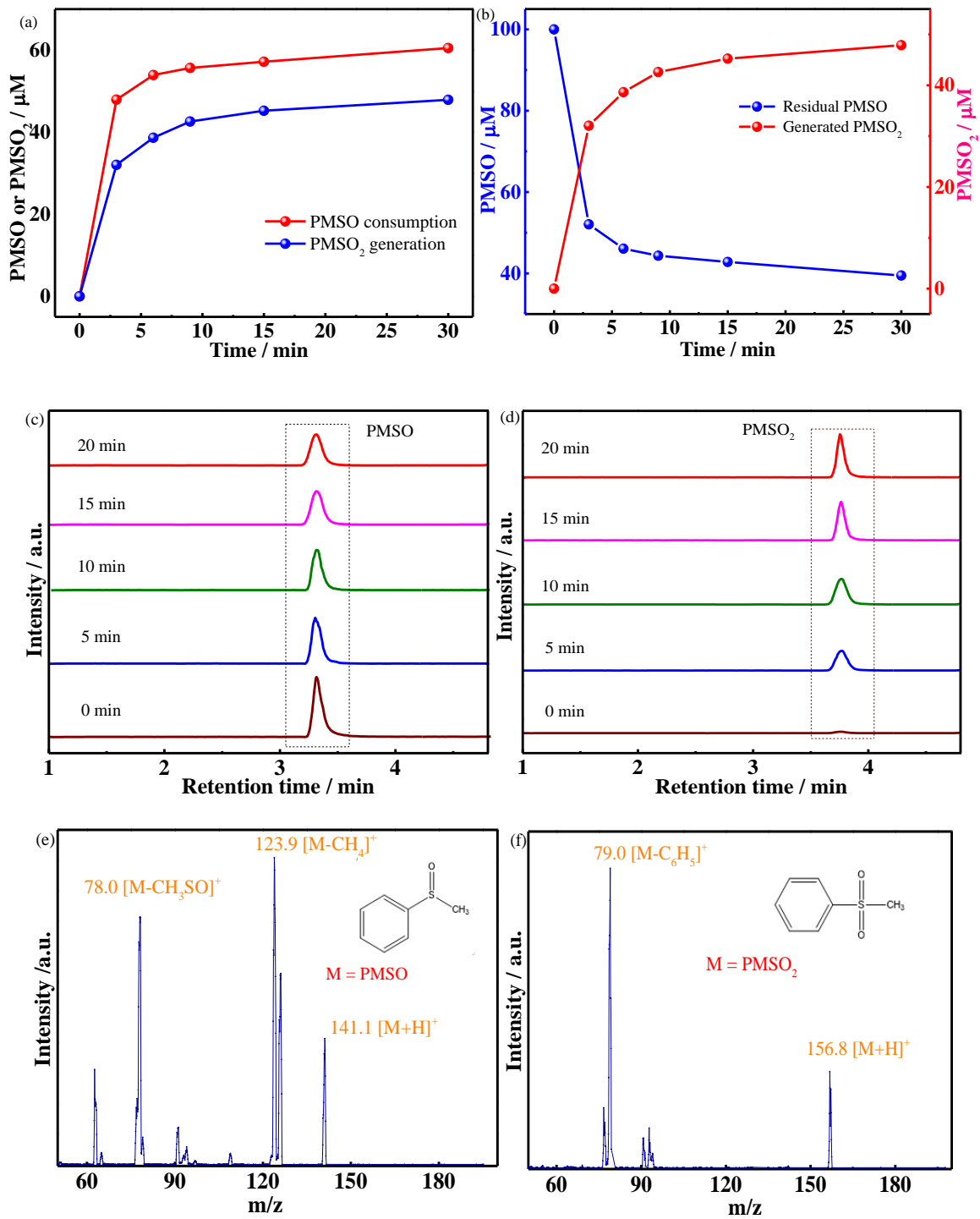


Figure S20. Catalytic activity, XRD pattern and TEM image of FeN_x-C-600 after HCl poisoned, Reaction conditions: catalyst dosage = 0.2 g/L, [PMS]₀ = 0.50 mM, [BPA]₀ = 20 mg/L, pH₀ = 6.5



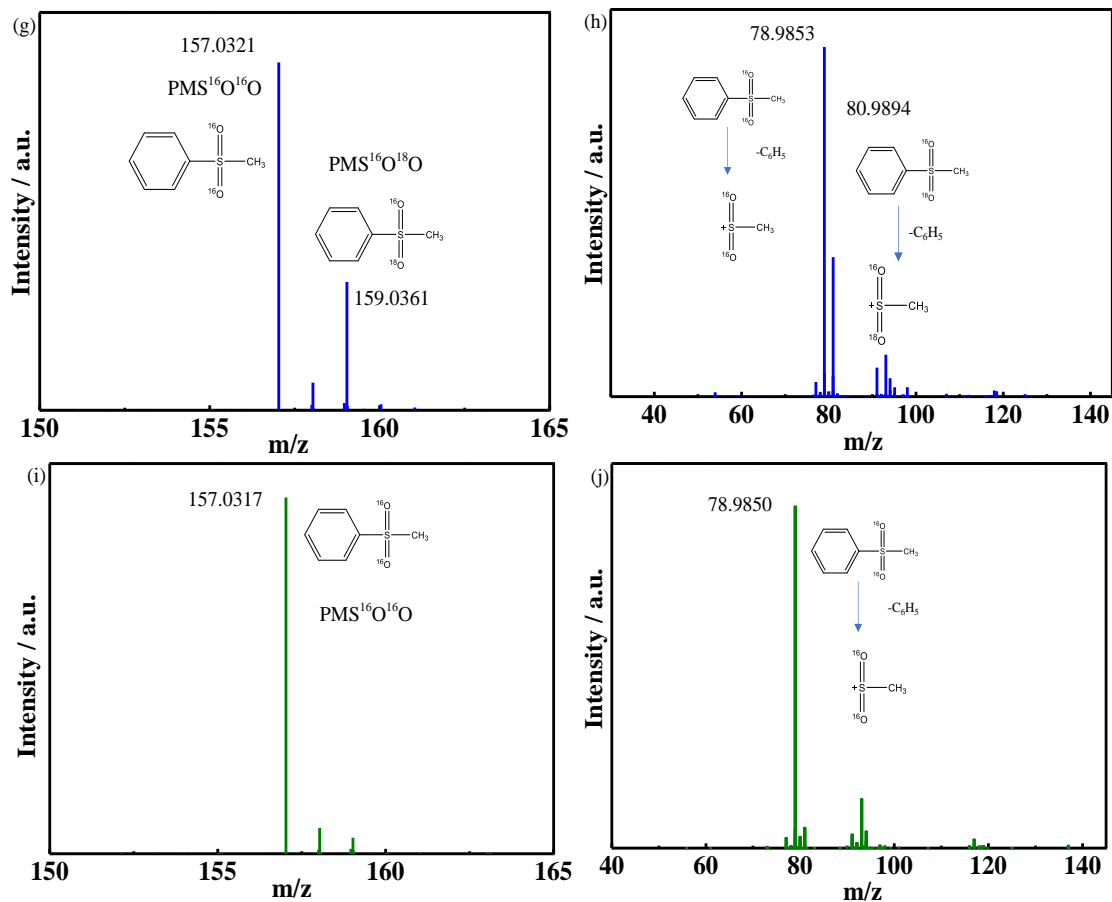


Figure S21. (a-d) PMSO consumption and PMSO₂ generation in the FeN_x-C-600/PMS/BPA system, (e-f) MS/MS spectra of PMSO and PMSO₂, (g-h) MS spectra of PMS¹⁶O¹⁶O/ PMS¹⁶O¹⁸O in FeN_x-C/PMS system and (i-j) MS spectra of PMS¹⁶O¹⁶O in PMS alone system; Reaction conditions: catalyst dosage = 0.2 g/L,

$$[\text{PMS}]_0 = 0.50 \text{ mM}, [\text{BPA}]_0 = 20 \text{ mg/L}, \text{pH}_0 = 6.5, [\text{PMSO}] = 10.0 \text{ }\mu\text{M}$$

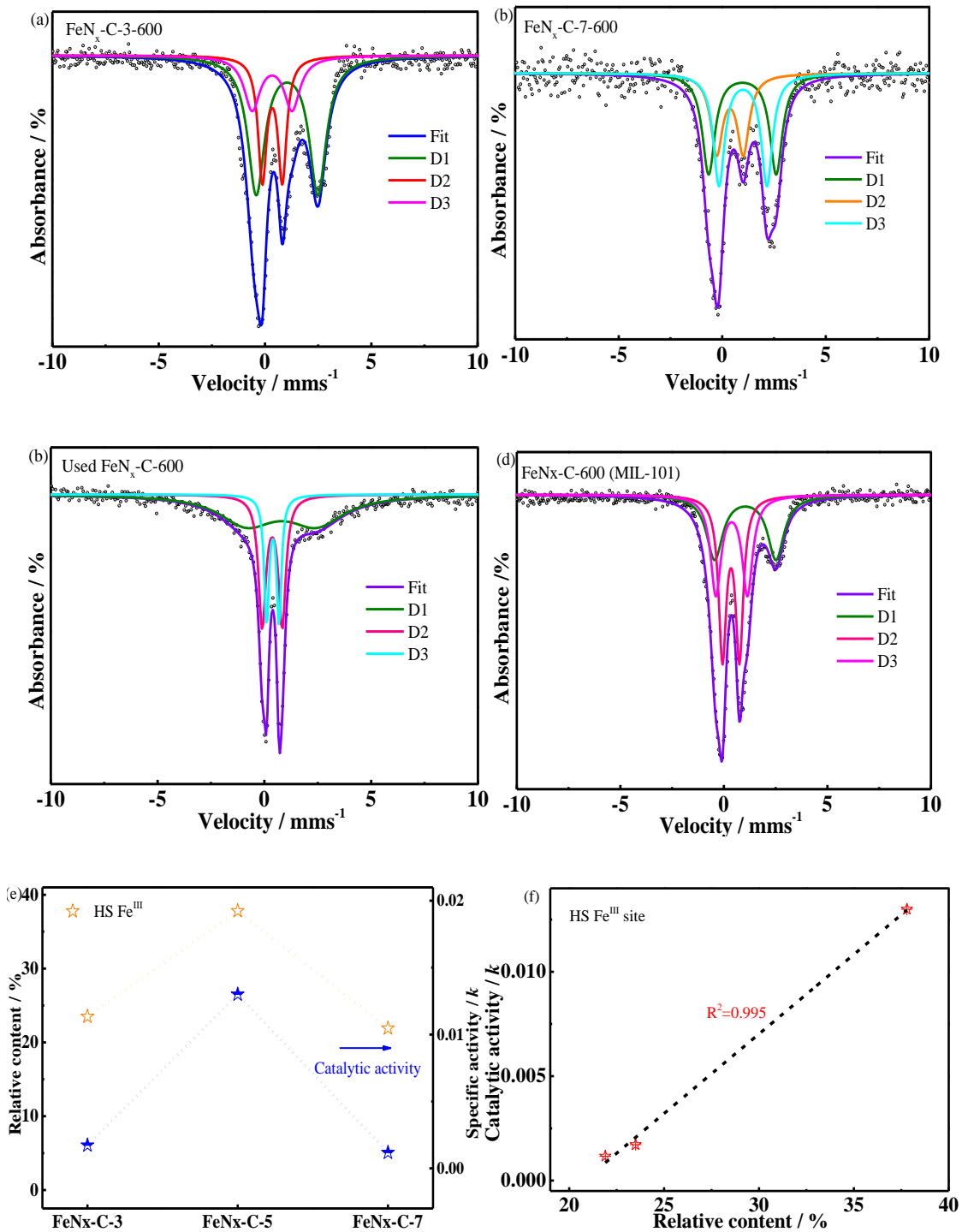


Figure S22. Fitted ^{57}Fe Mössbauer spectra of as-synthesized catalysts and the correlation between high spin ferric iron sites and catalytic activity

As depicted in Figure S22, all the high-spin Fe^{II}, low-spin Fe^{III} and high-spin Fe^{III} species can be detected in the FeN_x-C-3-600 sample, while the amount of each species was distinctly different from the FeN_x-C-5-600 sample (Table S7). Moreover, with further increasing the melamine dosage, the low-spin Fe^{III} species disappeared in the FeN_x-C-7-600 sample and the content of Fe^{II} phase increased. This result points to greater release of reducing gas (NH₃) via excessive melamine decomposition and rearrangement, which facilitates Fe^{III} species reduction to Fe^{II} during the pyrolysis process. According to the catalytic performance, sample FeN_x-C-5 exhibited higher catalytic efficiency than FeN_x-C-3 and FeN_x-C-7 under the same pyrolysis temperature (600°C), reflecting the distinct functions of different spin states of iron species towards PMS activation and BPA decontamination.

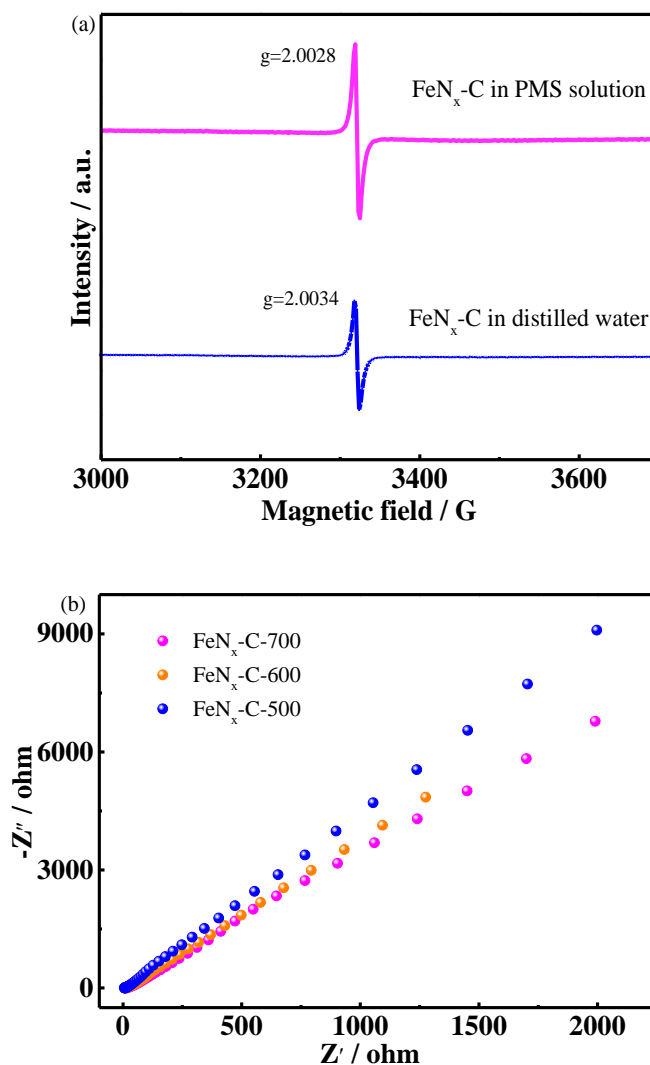


Figure S23. (a) EPR spectra of sample FeN_x-C-600 in distilled water and PMS solution under 77K; (b) EIS Nyquist plots of FeN_x-C-500, 600 and 700 catalysts

Electrochemical impedance spectroscopy indicated that sample FeN_x-C-600 generated a relatively small semicircle diameter compared with sample FeN_x-C-500, implying lower electron transfer resistance and higher conductivity. Furthermore, during the BPA decomposition processes, BPA tended to lose electrons and was thereby oxidized via the generated radical and nonradical species (high-valent Fe species). Therefore, the current and potential of the catalyst would experience certain variations in the oxidation process.

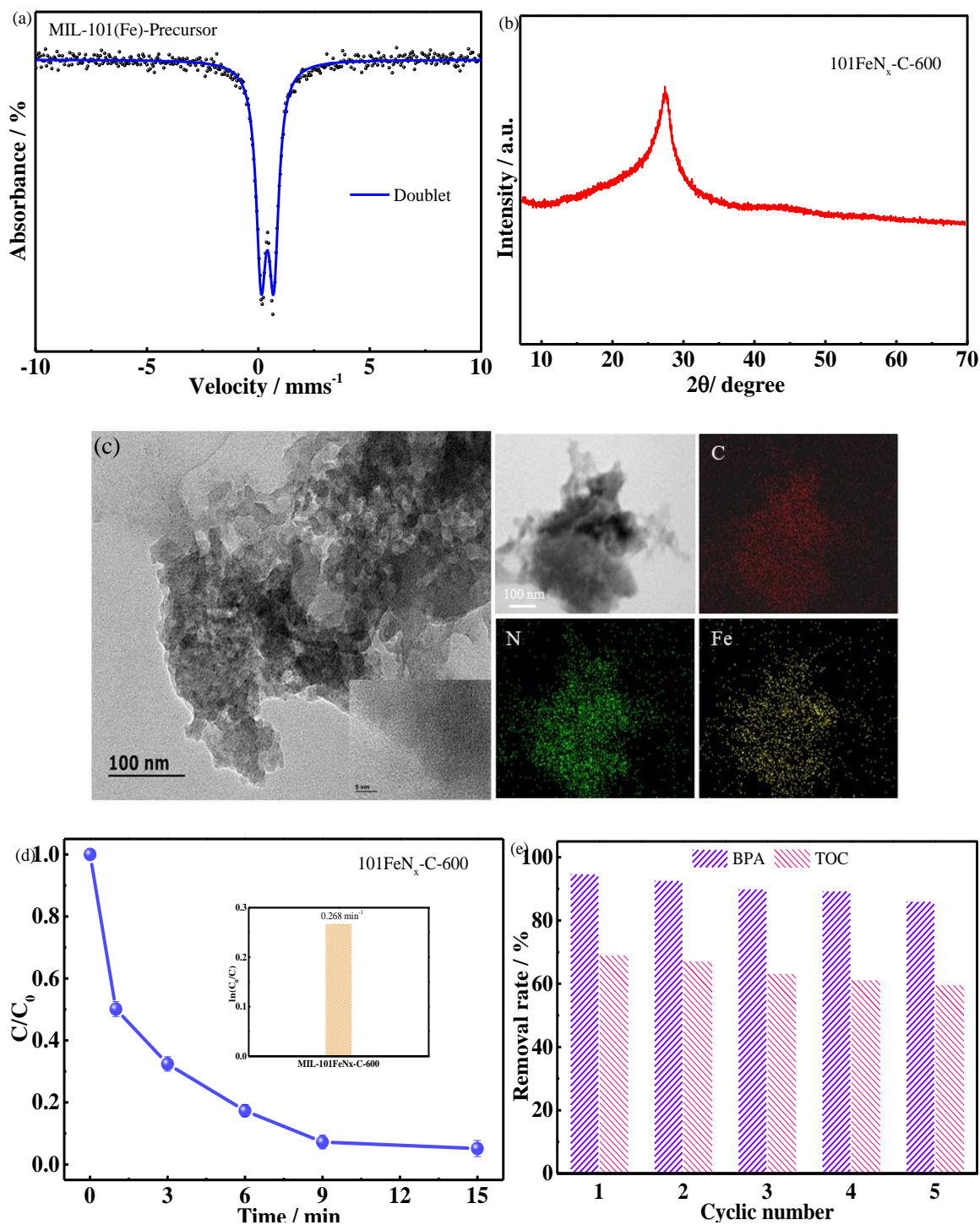


Figure S24. (a) Fitted ^{57}Fe Mössbauer spectra of MIL-101(Fe) precursor; (b) XRD pattern of $101\text{FeN}_x\text{-C-600}$ catalyst; (c) TEM images and EDS mapping of $101\text{FeN}_x\text{-C-600}$ catalyst; (d) Catalytic performance for BPA degradation; (e) Stability of $101\text{FeN}_x\text{-C-600}$ for BPA removal, Reaction conditions: catalyst dosage = 0.2 g/L,

$[\text{PMS}]_0 = 0.50 \text{ mM}$, $[\text{BPA}]_0 = 20 \text{ mg/L}$, $\text{pH}_0 = 6.5$

Specifically, the MIL-101(Fe) was fully mixed with melamine at a ratio of 1:5 and then transferred to a tube furnace and calcined at 600°C for 3 h under N₂ atmosphere. Subsequently, XRD, HRTEM, XAS and ⁵⁷Fe Mössbauer spectroscopy were performed. As depicted in Figure S23, only characteristic peaks located at 27.5 and 44.5° assigned to graphitic carbon were identified in the 101FeN_x-C catalyst. The absence of particles and distinct lattice distances in TEM and HRTEM images excluded the existence of iron-based nanoparticles and crystalline species. The coexistent and uniform distribution of Fe and N on the carbon support were illustrated by EDS elemental mapping. Furthermore, the edge energy of the Fe K-edge XANES spectrum of sample 101FeN_x-C is located between the edge energies of Fe foil and Fe₂O₃ (Figure 2a), indicating a positive valence state of 101FeN_x-C between 0 and +3. The EXAFS displayed a major peak at 1.5 Å, corresponding to the Fe-N shell. The best fitting parameters for the first coordination shell of 101FeN_x-C indicated an average Fe-N coordination number of 4.2 and 2.03 Å of Fe-N bond, indicating the successful construction of an atomic structure model of the 101FeN_x-C catalyst. As shown in Figure S23d-e, sample 101FeN_x-C exhibited a comparable catalytic efficiency to the MIL-53 based FeN_x-C catalyst and the TOC removal rate achieved 69.1%. Aside from the catalytic capacity, approximately 86.2% of bisphenol A removal can still be realized and the total leached iron was only 0.31 mg/L (far lower than the standard of 2.0 mg/L) after five cyclic experiments, illustrating the excellent stability of sample 101FeN_x-C.

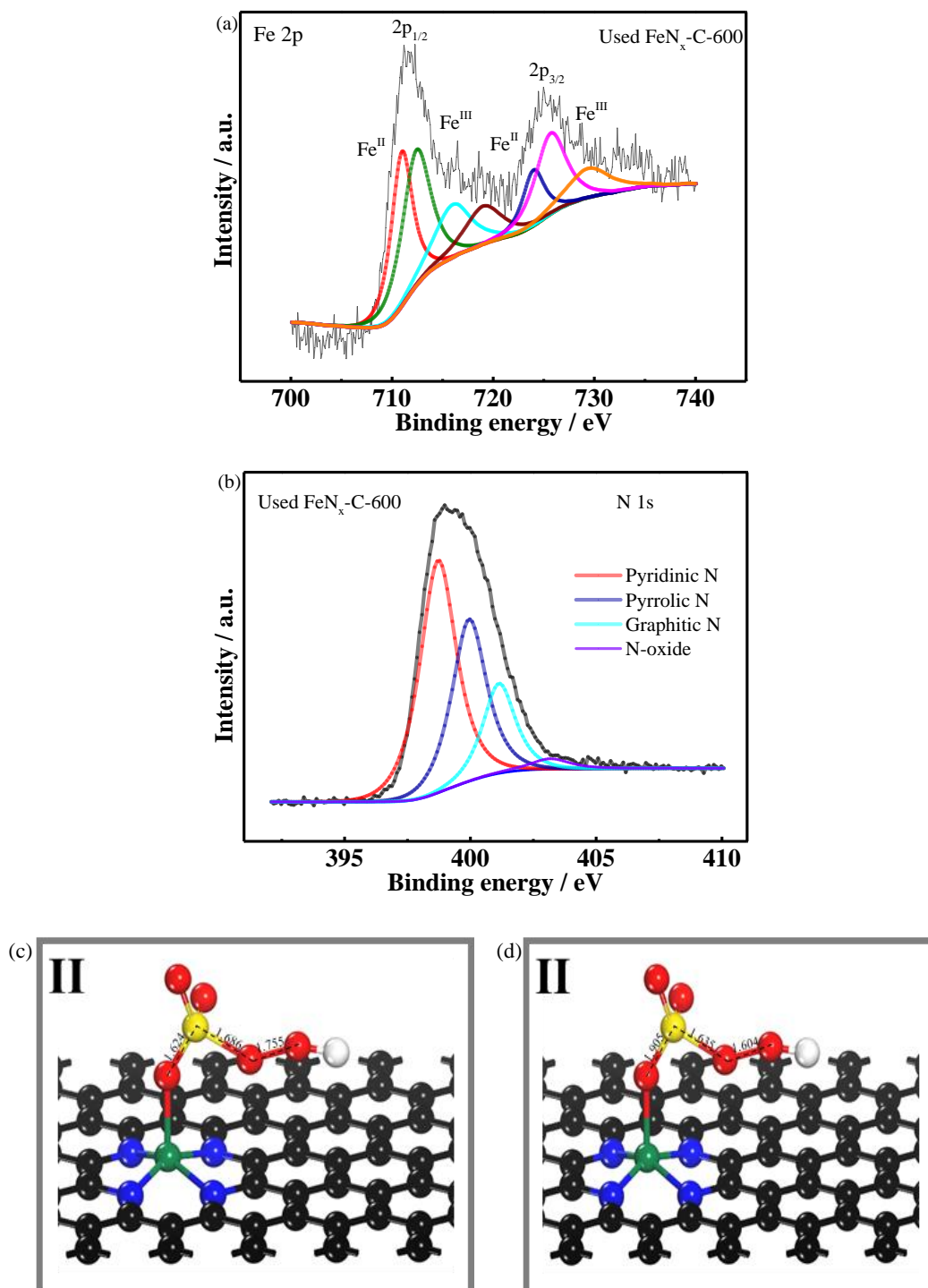


Figure S25. (a) Fe 2p and (b) N 1s XPS spectra of used FeN_x-C-600 catalyst; (c-d) *HSO₅ in different reaction process: (c) in Figure 5(c) *HSO₅-1; (b) in Figure 5(d) *HSO₅-2;

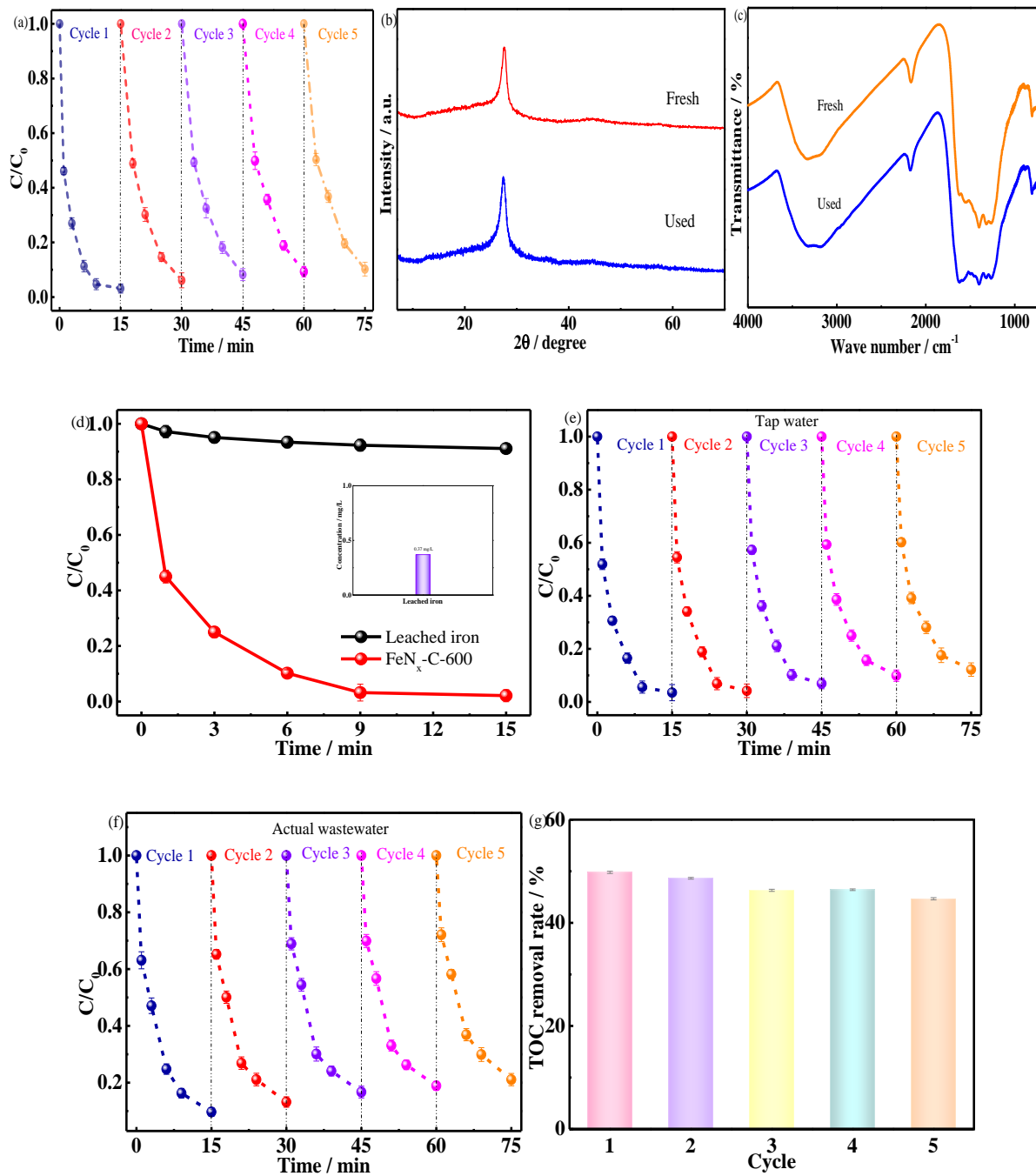


Figure S26. (a) Cycling experiment for BPA degradation; (b) XRD pattern; (c) FTIR spectra of Fe_{N_x}-C-600 catalyst; (d) Catalytic performance of leached iron towards BPA degradation; (e) BPA removal rate in tap water; (f) BPA removal rate in actual wastewater; (g) TOC removal rate in actual wastewater by Fe_{N_x}-C-600 catalyst over five cycles, Reaction conditions: catalyst dosage = 0.2 g/L, [PMS]₀ = 0.50 mM, [BPA]₀ = 20 mg/L, pH₀ = 6.5

Table S1. Structures and measurement parameters of various organic pollutants

Pollutants	Method	Chemical Formula
Phenol	<p>Measured by HPLC (C18 column 5 μm, 150 mm*4.6 mm). The mobile phase consisted of Methanol and water (70:30, v/v) at a flow rate of 0.8 mL/min with the detection wavelength at 280 nm. The column temperature was held at 25 ± 0.5 °C.</p>	$\text{C}_6\text{H}_6\text{O}$
Bisphenol A (BPA)	<p>Measured by HPLC (C18 column 5 μm, 150 mm*4.6 mm). The mobile phase consisted of Methanol and water (70:30, v/v) at a flow rate of 1.0 mL/min with the detection wavelength at 230 nm. The column temperature was held at 25 ± 0.5 °C. The degradation intermediates were obtained by HPLC-MS.</p>	$\text{C}_{15}\text{H}_{16}\text{O}_2$
Carbamazepine (CBZ)	<p>Measured by UV-vis with the detection wavelength at 285 nm.</p>	$\text{C}_{15}\text{H}_{12}\text{N}_2\text{O}$
Methylene Blue	<p>Measured by UV-vis with the detection wavelength at 665 nm.</p>	$\text{C}_{16}\text{H}_{18}\text{ClN}_3\text{S}$
Rhodamine B	<p>Measured by UV-vis with the detection wavelength at 554 nm.</p>	$\text{C}_{28}\text{H}_{31}\text{ClN}_2\text{O}_3$

Table S2. Iron content measured by ICP-OES and structural parameters of BET surface area, pore volume and pore size

Catalyst	Fe wt%	BET surface area (m ² /g)	Pore volume (cm ³ /g)	Average pore size (nm)
FeN _x -C-500	18.3	8.413	0.0271	8.23
FeN _x -C-600	5.91	135.2	0.327	8.32
FeN _x -C-700	35.2	460.6	0.907	7.84

Table S3. Structural parameters of the FeN_x-C-600 catalysts obtained from EXAFS fitting

Catalyst	Shell	Coordination number (N ^a)	Bond length R(Å) ^b	Bond disorder σ^2 (Å ²) ^c	R factor (%)
Fe foil	Fe-Fe1	8	2.47	0.0049	0.0006
	Fe-Fe2	6	2.85	0.0057	
FePc	Fe-N	4	1.98	0.0055	0.019
FeN _x -C-600 (MIL-53)	Fe-N	4.1	2.06	0.0080	0.020
FeN _x -C-600 (MIL-101)	Fe-N	4.2	2.03	0.0087	0.019

^aN, coordination number; ^bR, distance between absorber and backscatter atoms; ^c σ^2 , Debye-Waller factor

to account for both thermal and structural disorders; R factor indicates the goodness of the fit

Table S4. MS analysis of reaction intermediates during the degradation of BPA

<i>TP</i>	<i>Molecular formula</i>	<i>Structural formula</i>	<i>m/z</i>
TP1	C ₂ H ₆ O		46
TP2			
TP3	C ₇ H ₁₂		96
TP4	C ₆ H ₈ O		96
TP5	C ₆ H ₈ O ₂		112
TP6	C ₉ H ₁₀ O		134
TP7	C ₉ H ₁₂ O ₂		152
TP8	C ₈ H ₈ O ₃		
TP9	C ₁₄ H ₁₁ O		196
TP10	C ₁₅ H ₁₆ O ₂		227
TP11	C ₁₄ H ₁₆ O ₃		232
TP12	C ₁₅ H ₁₄ O ₃		242
TP13	C ₁₅ H ₁₂ O ₄		256
TP14	C ₁₅ H ₁₆ O ₄		260
TP15	C ₁₄ H ₁₂ O ₈		308

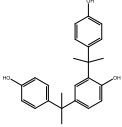
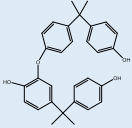
TP16	$C_{24}H_{26}O_3$		362
TP17	$C_{30}H_{30}O_4$		454
TP18	$C_{32}H_{34}O_4$		482

Table S5. Comparison of catalytic reactivity of FeN_x-C-600 catalyst with previous reported catalysts during

PMS activation							
Catalyst	Catalyst dosage (g L ⁻¹)	S _{BET} (m ² g ⁻¹)	Pollutant (mg L ⁻¹)	Removal rate (%)	Rate constant (min)	Specific activity (L min ⁻¹ m ⁻²)	Ref.
Fe/NCNFs-9	0.4	327	BPA/20	100	0.94	0.007	5 ⁶
NoCNT-700	0.1	450.0	Phenol/20	100	0.247	0.005	6 ⁷
NCNTFs	0.05	410.0	BPA/25	97	0.216	0.010	7 ⁸
NC-900	0.2	331.99	BPA/23	90	0.46	0.007	8 ⁹
NGC-700	0.1	1236.0	BPA/20	100	1.05	0.008	9 ¹⁰
NG	0.2	99.3	Phenol/20	100	0.071	0.003	10 ¹¹
FeSA-N-C	0.4	586.9	BPA/20	99	0.24	0.001	11 ¹²
AC/g-C3N4	1.0	192	Atrazine/5	96	0.0376	0.0002	12 ¹³
FeSA-N/C	0.15	522.3	BPA/20	99	0.317	0.004	13 ¹⁴
Fe0.5-N-C	0.1	215.2	BPA/10	97	0.0556	0.002	14 ¹⁵
Fe-N-BC	0.2	362.5	Acid range/20	98	0.114	0.001	15 ¹⁶
FeN _x -C-600	0.2	135.2	BPA/20	99	0.357	0.013	This work

Table S6. Parameters of industrial wastewater sample

Parameters	
pH	7.1~7.9
BOD	120
COD	66
TOC	12
Suspended solid	58
Phenolic	< 0.1
Cu	< 0.1
Fe	< 0.1
Zn	< 0.1
Mn	< 0.1

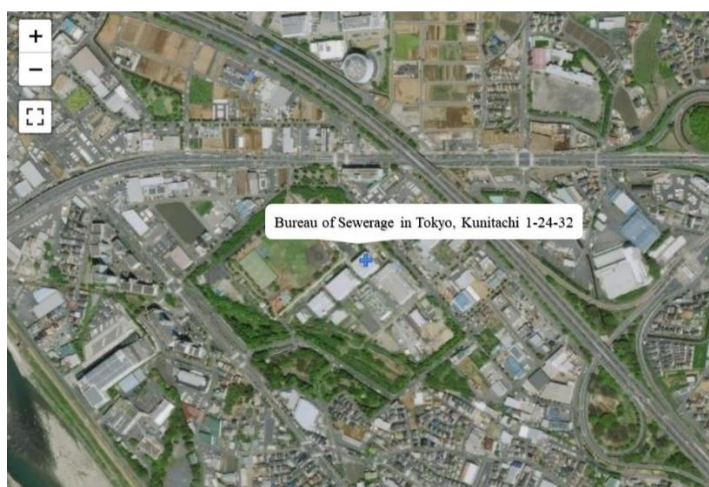


Table S7. Summary of the fitted ^{57}Fe Mössbauer parameters and assignments to different Fe species

Catalyst	Component	IS/mms ⁻¹	QS/mms ⁻¹	H ₀ /T	Area/%	Assignment
FeNx-C-500	D1	0.937	3.041		25.8	Fe ^{II} -N ₄ , HS
	D2	1.001	2.52		74.2	Fe ^{II} , HS
FeNx-C-600	D1	0.974	3.021		50.5	Fe ^{II} -N ₄ , HS
	D2	0.345	0.933		37.8	Fe ^{III} -N ₄ , HS
	D3	0.374	1.667		11.7	Fe ^{III} -N ₄ , LS
	Singlet	-0.0625			1.6	Fe ⁰ (Super-paramagnetic Fe)
FeNx-C-700	Sext	0.186		19.6	44.4	Fe ₃ C
	D1	0.277	1.048		22.0	Fe ^{III} , HS
	D2	0.319	2.505		32.0	Pc-type Fe ^{II} , intermediate-spin
FeNx-C-3-600	D1	0.999	2.951		49.3	Fe ^{II} , HS
	D2	0.345	0.937		23.5	Fe ^{III} , HS
	D3	0.355	1.867		27.2	Fe ^{III} , LS
FeNx-C-7-600	D1	0.975	3.263		40.7	Fe ^{II} , HS
	D2	0.375	1.284		21.9	Fe ^{III} , HS
	D3	1.003	2.311		37.4	Fe ^{II} , HS
FeNx-C-600-Low temperature	D1	1.19	3.166		31.6	Fe ^{II} -N ₄ , HS
	D2	0.394	1.764		16.4	Fe ^{III} -N ₄ , LS
	D3	0.458	0.971		52.0	Fe ^{III} -N ₄ , HS
FeNx-C-600-used	D1	0.810	3.28		50.0	Fe ^{II} -N ₄ , HS
	D2	0.365	0.937		30.6	Fe ^{III} -N ₄ , HS
	D3	0.395	0.584		19.4	Fe ^{III} -N ₄ , HS

101Fe- FeNx-C-600	D1	1.033	2.960	31.5	Fe ^{II} -N ₄ , HS
	D2	0.343	0.818	37.0	Fe ^{III} -N ₄ , HS
	D3	0.374	1.525	31.5	Fe ^{III} -N ₄ , LS
MIL- 101(Fe)	D1	0.408	0.562	100.0	Octahedral Fe ^{III}

References

1. Xing, D.; Cui, Z.; Liu, Y.; Wang, Z.; Wang, P.; Zheng, Z.; Cheng, H.; Dai, Y.; Huang, B. Two-dimensional π -d conjugated metal-organic framework $\text{Fe}_3(\text{hexaiminotriphenylene})_2$ as a photo-Fenton like catalyst for highly efficient degradation of antibiotics. *Appl. Catal., B* **2021**, *290*, 120029.
2. An, S.; Zhang, G.; Wang, T.; Zhang, W.; Li, K.; Song, C.; Miller, J. T.; Miao, S.; Wang, J.; Guo, X. High-Density Ultra-small Clusters and Single-Atom Fe Sites Embedded in Graphitic Carbon Nitride ($\text{g-C}_3\text{N}_4$) for Highly Efficient Catalytic Advanced Oxidation Processes. *ACS Nano* **2018**, *12*, 9441-9450.
3. Xing, Y.; Yao, Z.; Li, W.; Wu, W.; Lu, X.; Tian, J.; Li, Z.; Hu, H.; Wu, M. Fe/ Fe_3C Boosts H_2O_2 Utilization for Methane Conversion Overwhelming O_2 Generation. *Angew. Chem., Int. Ed. Engl.* **2021**, *60*, 8889-8895.
4. Ahmadi, M.; Ghanbari, F. Combination of UVC-LEDs and ultrasound for peroxymonosulfate activation to degrade synthetic dye: influence of promotional and inhibitory agents and application for real wastewater. *Environ. Sci. Pollut. Res.* **2018**, *25*, 6003-6014.
5. Qian, K.; Chen, H.; Li, W.; Ao, Z.; Wu, Y. N.; Guan, X. Single-Atom Fe Catalyst Outperforms Its Homogeneous Counterpart for Activating Peroxymonosulfate to Achieve Effective Degradation of Organic Contaminants. *Environ. Sci. Technol.* **2021**, *55*, 7034-7043.
6. Chen, S.; Li, M.; Zhang, M.; Wang, C.; Luo, R.; Yan, X.; Zhang, H.; Qi, J.; Sun, X.; Li, J. Metal organic framework derived one-dimensional porous Fe/N-doped carbon nanofibers with enhanced catalytic performance. *J. Hazard. Mater.* **2021**, *416*, 126101.
7. Duan, X.; Sun, H.; Wang, Y.; Kang, J.; Wang, S. N-Doping-Induced Nonradical Reaction on Single-Walled Carbon Nanotubes for Catalytic Phenol Oxidation. *ACS Catal.* **2015**, *5*, 553-559.
8. Ma, W.; Wang, N.; Fan, Y.; Tong, T.; Han, X.; Du, Y. Non-radical-dominated catalytic degradation of bisphenol A by ZIF-67 derived nitrogen-doped carbon nanotubes frameworks in the presence of peroxymonosulfate. *Chem. Eng. J.* **2018**, *336*, 721-731.
9. Gao, Y.; Zhu, Y.; Chen, Z.; Zeng, Q.; Hu, C. Insights into the difference in metal-free activation of peroxymonosulfate and peroxydisulfate. *Chem. Eng. J.* **2020**, *394*, 123936.

10. Luo, R.; Li, M.; Wang, C.; Zhang, M.; Nasir Khan, M. A.; Sun, X.; Shen, J.; Han, W.; Wang, L.; Li, J. Singlet oxygen-dominated non-radical oxidation process for efficient degradation of bisphenol A under high salinity condition. *Water Res.* **2019**, *148*, 416-424.
11. Wang, C.; Kang, J.; Sun, H.; Ang, H. M.; Tadó, M. O.; Wang, S. One-pot synthesis of N-doped graphene for metal-free advanced oxidation processes. *Carbon* **2016**, *102*, 279-287.
12. Li, Y.; Yang, T.; Qiu, S.; Lin, W.; Yan, J.; Fan, S.; Zhou, Q. Uniform N-coordinated single-atomic iron sites dispersed in porous carbon framework to activate PMS for efficient BPA degradation via high-valent iron-oxo species. *Chem. Eng. J.* **2020**, *389*, 124382.
13. Dangwang Dikdim, J. M.; Gong, Y.; Noumi, G. B.; Sieliechi, J. M.; Zhao, X.; Ma, N.; Yang, M.; Tchatchueng, J. B. Peroxymonosulfate improved photocatalytic degradation of atrazine by activated carbon/graphitic carbon nitride composite under visible light irradiation. *Chemosphere* **2019**, *217*, 833-842.
14. Yang, T.; Fan, S.; Li, Y.; Zhou, Q. Fe-N/C single-atom catalysts with high density of Fe-N_x sites toward peroxymonosulfate activation for high-efficient oxidation of bisphenol A: Electron-transfer mechanism. *Chem. Eng. J.* **2021**, *419*, 129590.
15. Xu, L.; Fu, B.; Sun, Y.; Jin, P.; Bai, X.; Jin, X.; Shi, X.; Wang, Y.; Nie, S. Degradation of organic pollutants by Fe/N co-doped biochar via peroxymonosulfate activation: Synthesis, performance, mechanism and its potential for practical application. *Chem. Eng. J.* **2020**, *400*, 125870.
16. Li, X.; Jia, Y.; Zhou, M.; Su, X.; Sun, J. High-efficiency degradation of organic pollutants with Fe, N co-doped biochar catalysts via persulfate activation. *J. Hazard. Mater.* **2020**, *397*, 122764.